ANALYSES OF SEA SURFACE HEIGHT, BOTTOM PRESSURE AND

ACOUSTIC TRAVEL TIME IN THE JAPAN/EAST SEA

BY

YONGSHENG XU

A DISSERTATION SUBMITTED IN PARTIAL FULFILLMENT OF THE

REQUIREMENTS FOR THE DEGREE OF

DOCTOR OF PHILOSOPHY

IN

OCEANOGRAPHY

UNIVERSITY OF RHODE ISLAND

2006

Report Documentation Page

1. REPORT DATE **2006**	2. REPORT TYPE	3. DATES COVERED **00-00-2006 to 00-00-2006**

4. TITLE AND SUBTITLE	5a. CONTRACT NUMBER
Analyses of Sea Surface Height, Bottom Pressure and Acoustic Travel Time in the Japan/East Sea	5b. GRANT NUMBER
	5c. PROGRAM ELEMENT NUMBER
6. AUTHOR(S)	5d. PROJECT NUMBER
	5e. TASK NUMBER
	5f. WORK UNIT NUMBER

7. PERFORMING ORGANIZATION NAME(S) AND ADDRESS(ES) **University of Rhode Island,Graduate School of Oceanography,Narragansett,RI,02882**	8. PERFORMING ORGANIZATION REPORT NUMBER

9. SPONSORING/MONITORING AGENCY NAME(S) AND ADDRESS(ES)	10. SPONSOR/MONITOR'S ACRONYM(S)
	11. SPONSOR/MONITOR'S REPORT NUMBER(S)

12. DISTRIBUTION/AVAILABILITY STATEMENT
Approved for public release; distribution unlimited

13. SUPPLEMENTARY NOTES

14. ABSTRACT
see report

15. SUBJECT TERMS

16. SECURITY CLASSIFICATION OF:			17. LIMITATION OF ABSTRACT	18. NUMBER OF PAGES	19a. NAME OF RESPONSIBLE PERSON
a. REPORT **unclassified**	b. ABSTRACT **unclassified**	c. THIS PAGE **unclassified**	**Same as Report (SAR)**	**99**	

DOCTOR OF PHILOSOPHY DISSERTATION

OF

YONGSHENG XU

APPROVED:

Dissertation Committee:

Major Professor

_____

_____

_____

_____
DEAN OF THE GRADUATE SCHOOL

UNIVERSITY OF RHODE ISLAND

2006

ABSTRACT

The observed water motions in the Japan/East Sea (JES) and the associated sea surface height and bottom pressure fields are heavily influenced by the semi-enclosed nature and the specific configuration of this marginal sea. As part of the United States Office of Naval Research JES program, a two-dimensional array of pressure-gauge-equipped inverted echo sounders (PIESs) was deployed in the southwestern JES for two years, from June 1999 to July 2001. The PIESs recorded hourly vertical acoustic travel time and pressure, which are respectively good proxies of baroclinic and barotropic sea level variability. Three topics are investigated based on the PIES data sets: (1) implications of the in-situ measurements for improving interpretation of satellite altimetric data in the JES; (2) basin-mode oscillations in the JES; (3) vertical coupling between upper circulation and abyssal eddy fields in the JES.

All the pressure records exhibit a strong remarkably similar signal (common mode). The common mode is driven by sea level changes outside the JES, atmospheric pressure, and along-strait wind stress in the straits connecting the JES to the outside ocean. The common mode has a barotropic wavelength much larger than the size of the JES, so it is in phase throughout the basin. The rms of the common mode is about 5 cm, and is energetic at time scales of 2-70 days, which are shorter than the ERS-2 satellite altimetry Nyquist period of 70 days. Our results show the common mode produces a substantial alias when sampled by satellite altimeter; furthermore, the combined aliasing effects on multi-tracks can mimic mesoscale eddies and may qualitatively alter the synoptic mapping. The alias can be suppressed by removing the common mode from satellite SSH. For time periods other than 1999-2001, 78% of the common mode variance can still be removed in the Japan/East Sea by using coastal tide gauge data to infer the common mode.

High frequency oscillations with period around 7 hours are shown to be organized in a fundamental basin mode in the JES. The semi-enclosed nature of the JES not only accounts for the existence of the common mode signal but also limits energy propagation away from the basin and constrains its free oscillations to discrete modes. The fundamental oscillation in the JES is determined by its boundaries and topography. Influenced by the rotation of the earth, the oscillation consists of a single amphidromic point around which the high water propagates counter-clockwise. It has a period of 7 hours with along-coast wavelength equal to the circumference of the basin. The basin oscillations have largest amplitude at the narrow northeast region of the JES. The time series of basin oscillations is modulated in packets with time scales of 2-16 days, and they also exhibit a seasonal modulation. Wind in the direction $60°/240°$T is optimal to generate basin oscillations in the Japan/East Sea.

Vertical-coupled patterns between upper sea surface height and abyssal pressure field are investigated. The coupled mode analysis confirms that bottom topography has a significant influence on the vertical coupling in the Japan/East Sea. In the first coupled mode, the deep response flows are largely expressed on closed potential vorticity regions created by the Ulleung Basin depression or the Korea Plateau; the upper layer exhibits a migration of the Ulleung Warm Eddy and downstream shift of a meander trough of the Subpolar Front. In the second mode, the upper and deep layer have similar spatial patterns peaked at a site near the southwestern corner of the Korea plateau. The second mode appears to arise from time-varying strength of a mean deep anticyclone, which had been revealed by intermediate float data, flowing around the contours of the Korea Plateau.

ACKNOWLEDGMENTS

TABLE OF CONTENTS

APPENDIX

LIST OF TABLES

LIST OF FIGURES

x

xi

MANUSCRIPT 1

Improving Sea-Level Estimates from Satellite Altimetry Using In Situ Measurements in the Japan / East Sea

Abstract

We investigate implications of in-situ measurements to improve interpretation of satellite altimetric data in the Japan/East Sea. Along-track and merged sea level anomaly products from TOPEX/Poseidon (T/P) and ERS-2 are compared in this marginal sea with data from a two-dimensional moored array of 23 pressure-recording inverted echo sounders (PIESs). Sea level spatio-temporal correlation scales are derived using PIES nearly-continuous temporal sampling and spatially-extensive altimeter measurements. Total changes of sea level in the Japan/East Sea are the sum of baroclinic variability (6.6 cm rms) and barotropic variability (5.0 cm rms). Bottom pressure represents the inverse barometer corrected barotropic sea level variability, which is dominated by a nearly uniform signal among all PIES sites; it serves as a proxy for a common mode sea level variation throughout the Japan/East Sea. The common mode contains energetic short period fluctuations at periods < 70 days, producing an alias, which accounts for 37% of the errors in the merged (T/P and ERS-2) product. The common mode can not only lead to 'trackiness' errors among neighboring and crossing tracks, but also to false SSH topographic highs (or lows) in altimeter mapped products. The alias can be well suppressed by subtracting the common mode estimated from bottom pressure. Alternatively 78% of the common mode variance can be removed in the Japan/East Sea by using coastal tide gauge data.

1.1   Introduction

The Japan/East Sea (JES) is a deep, semi-enclosed marginal sea surrounded by Korea, Russia, and Japan. Exchange with the surrounding seas is restricted by narrow passages with sill depths not exceeding 150 m. The observed water motions and associated sea level variations are heavily influenced by the response of this semi-enclosed marginal sea to external and atmospheric forcing [Chang et al, 2004].

Observations from satellite altimeters have provided global descriptions of sea level variability during the past three decades. The uncertainty of satellite altimetry data in a semi-enclosed sea may typically be double that of open oceans because of lower accuracy in corrections, e.g., for tides (Monique Gasc, AVISO, personal communication). Although the merged sea level anomaly (SLA) product from several satellites provides better resolution of mesoscale variability, energetic (uncorrected) high frequency variability can lead to large aliasing error in satellite altimeter observations. Most former comparisons of altimetric SLA with in situ measurements have been conducted in the open ocean. Assessing the sampling and accuracy of altimeter sea level measurements against in situ measurements in marginal seas is a required step towards improving interpretation of altimeter data in those regions.

As part of the United States Office of Naval Research JES program, a two-dimensional array of pressure-gauge-equipped inverted echo sounders (PIESs) was deployed in the southwestern JES for two years, from June 1999 to July 2001. The PIESs recorded vertical acoustic travel time and bottom pressure hourly, from which SLA is derived [Hendry et al, 2002; Teague et al, 1995].

Several processes in the JES cause its sea level variations to differ from the open ocean. Basin-scale barotropic sea level variation is driven by sea level changes

outside the JES, atmospheric pressure, and along-strait wind stress [Lyu and Kim, 2005]. We will show in section 1.3.1 that the contribution of these barotropic components is about 5 cm rms. All the detided bottom pressure (BP) records (barotropic signals) were dominated by a uniform signal [Park and Watts, 2005]. The barotropic mode wavelength is much larger than the size of the JES, so this signal is in phase throughout the basin as a "common mode". We use the average of our BP measurements as a proxy of this common mode signal throughout the JES.

We will show that the common mode combines with the large scale steric signal to produce a spatial correlation function that remains above 0.5 even at 300 km distance in the JES. In contrast, Morimoto et al. [2000b] reported the mapped eddy field is over-smoothed with a 150 km correlation scale in the JES. Eddy features of several 10's to more than 100 km are commonly observed in the Ulleung basin (UB). For example, Mitchell et al. [2005] reported a cold-core eddy, referred to as the Dok Cold Eddy, which is about 60 km in diameter and formed repeatedly southwest of Dok Island. From the satellite-determined track of a drifter, Lie et al. [1995] determined that eddies in the UB characteristically have major and minor axes of about 120 km and 70 km. In a hydrographic survey east of Ulleung Island, Byun et al. [1997] showed a warm-core eddy with 100 km scale.

The combination of the PIES nearly-continuous temporal sampling with extensive altimeter measurements provides a good opportunity to derive for this region the temporal and spatial correlation scales. These are essential for optimal mapping, ocean data assimilation, and design of an effective observing system [Ducet and Le Traon, 2000].

The common mode variations that have periods shorter than 70 days can

produce aliasing error in satellite altimetric observations. Stammer et al. [2000] reported that even in the open ocean high frequency barotropic motions exist, and lead to large aliasing error in altimeter SLA. In the JES, Nam et al. [2004] illustrated the aliasing that arises from nonisostatic sea level response to atmospheric pressure, which accounts for 10% of the common mode variance. Nevertheless, the aliasing effect of the common mode does not seem to have been widely recognized even though it is potentially the largest source of aliasing error in the JES.

This study reveals several significant implications of in-situ measurements for altimetric data interpretation in the JES. T/P and ERS-2 along-track and merged SLA products are compared with coincident SLA from in-situ PIES measurements. Space and time scales are derived using complementary altimetry and PIES measurements. The common mode alias will be shown to produce qualitatively wrong spatial features in synoptic mapping of SLA, and we will show how to suppress the common mode aliasing in satellite observations using bottom pressure or coastal tide gauge measurements.

1.2 Data Sources

PIES site locations, and T/P and ERS-2 tracks are shown in Figure 1.1. The PIES is an ocean bottom moored instrument that hourly measures BP and the time for an acoustic pulse to travel from the sea floor to the ocean surface and back. The acoustic travel time is an integral quantity that depends on the sound-speed profile of the water column. Appendix A discusses the interpretation and accuracy of acoustic travel time measurements. The baroclinic (steric) component of the sea level, geopotential anomaly relative to 500 dbar level was converted from acoustic travel time and sea surface temperature by a lookup table of specific volume anomaly [Park et al., 2005]. The acoustic travel time data were 120-hour low-pass filtered before the conversion. This filters out small spatial scale baro-

clinic variability to compare against the along-track filtered AVISO SLA product. The BP records were leveled geostropically relative to deep current meter records obtained from a correlated array in this experiment. They were accurately detided using the Munk and Cartwright [1966] tidal response analysis technique. The BP was not low pass filtered because the BP is dominated by large scale high frequency variability in the JES. Details on the processing of the pressure records are provided in a PIES data report [Mitchell et al., 2004b]. The barotropic (non-steric) component of the sea level was obtained from the BP using the hydrostatic approximation. The sum of the baroclinic and barotropic sea-level components gives the total sea level height:

$$H = \frac{\phi}{g} + \frac{P}{\rho g} \qquad (1.1)$$

where ϕ (m^2/s^2) is geopotential anomaly relative to 500 dbar depth representing the 'steric' or baroclinic component, g (9.8 m^2/s) is gravity, P (N/m^2) is bottom pressure (the barotropic component), ρ (1036 kg/m^3) is typical deep sea water density. Only the departure from isostatic or inverted barometer (IB) response contributes to the bottom pressure signals. Thus, BP does not change when sea level responds isostatically to atmospheric forcing. The barotropic altimeter SLA, corrected for IB response, is consistent with BP.

Hourly measured tide gauge (TG) data from 1999 through 2001 at sites inside the JES (Figure 1.1) were collected from the Japan Oceanographic Data Center and the Korean National Fisheries Research and Development Institute. The reanalyzed atmospheric pressure data come from the Navy Operational Global Atmospheric Prediction System (NOGAPS). They are on a one degree grid with time interval 12 hours.

The T/P and ERS-2 along-track and gridded SLA products published by

5

AVISO were produced by the CLS Space Oceanography Division as part of the Environment and Climate EU ENACT project (EVK2-CT2001-00117) and with support from CNES. T/P and ERS-2 data have a repeat period of 9.92 days and 35 days, respectively. The sea level anomaly product was obtained from AVISO reprocessed T/P and ERS-2 data, as described in detail in the SSALTO/DUACS User Handbook [2004]. Besides the standard corrections for (tides with the GOT99 tidal model), inverse barometer, radiometer, and electromagnetic bias, additional corrections involving subsampling, filtering, and long-wave corrections had been made. In Section 5 only, to illustrate common mode aliasing and de-aliasing in altimeter observations, we use the along-track data without long-wave correction to avoid missing part of the common mode signal. The merged data (T/P + ERS-2) used in this paper have a 7-day temporal resolution, a $1/3 \times 1/3$ degree spatial resolution, and cover the period from June 1999 to June 2001.

For this study, we extracted the altimeter data from June 1999 through June 2001, and all time series of SLA are calculated relative to the time average over this two-year period.

1.3 Sea Level Variation from Satellite Altimetry and PIES Measurements

1.3.1 Comparison of Along-track SLA Product and PIES Measurements

Coincident measurements of sea-level from PIESs and satellite altimeters were compared at all sites spaced less than 10 km from at least one satellite ground track. The PIES measurements were temporally subsampled to coincide within 1/2 hour with the altimeter measurements. Since the PIESs were deployed for 734 days, each of these PIES sites offered respectively 73 or 20 comparisons with T/P or ERS-2 passes.

Figure 1.2 shows time series pairs of SLA between T/P ($H_{T/P}$), ERS-2 (H_{ERS-2}), and PIES (H_{PIES}) at sites P1-6 and P2-4. The distances from these two PIES sites to the closest T/P and ERS-2 ground tracks are 1.02 km and 0.58 km respectively. H_{PIES} generally agrees well with $H_{T/P}$ and H_{ERS-2} at the two sites, and respective correlations R are 0.93 and 0.94. The panels in the right column exhibit barotropic and baroclinic components of H_{PIES}. The baroclinic components at the two sites show relatively low frequency variations and differ greatly from each other. On the other hand, the rms of barotropic components at the two sites exhibit a uniform signal (about 5 cm rms). A proxy for the common mode was constructed by averaging three pressure records (P2-3, P3-3, P5-5) that displayed undetectable sensor drift, and good signal-to-noise ratio.

For the PIES sites within 10 km of T/P tracks (P1-1, P1-6 and P3-2) the correlation coefficients range from 0.71 to 0.93; for corresponding PIES sites close to ERS-2 tracks (P1-4, P2-2, P2-4, P2-5, P3-1, P4-2, P4-3 and P2-5) the correlation coefficients range from 0.68 to 0.94. The lowest correlation (0.68) occurs at site P3-1 located at the shelf break. The low correlation may arise from lateral uncertainty of ERS-2 tracks where the geoid is steep.

Figure 1.3 shows the scatterplots of all data pairs, H_{PIES} versus $H_{T/P}$ (left panel) and H_{ERS-2} (right panel). The scatterplots yield an rms difference of 4.7 cm and correlation of 0.89 for T/P, while the corresponding values for ERS-2 are 5.1 cm and '0.85. The primary source of error in H_{PIES} is in the conversion of the acoustic travel times to geopotential height. This error is about 2.5 cm in the southwestern JES [Mitchell et al., 2004a; Park et al., 2005]. The approximate uncertainty of altimeter SLA in this region may be estimated from the residual $(4.72^2 - 2.52^2)^{1/2} = 4.0$ cm for T/P, and $(5.12^2 - 2.52^2)^{1/2} = 4.4$ cm for ERS-2.

These uncertainties in altimeter SLA in the JES are larger than in open oceans,

partly because the tide correction in the altimeter data is worse. The tide correction from the global model has less accuracy in a marginal sea such as the JES [Morimoto et al, 2000a]. In the next section, we will show that the residual tide signal is a substantial error source for the AVISO altimeter SLA product in the JES.

1.3.2 Comparison of Merged SLA Product and PIES Measurements

We next compare the AVISO merged SLA product against all 23 PIES sites. We found that the merged SLA data contain little variance at periods shorter than 30 days in this region. Consequently, a low-pass filter was applied on the PIES data that improves correlations by eliminating signals shorter than 30 days (H_{PIESLP}). The merged SLA data (H_{MAP}) at 7-day interval were spatially interpolated to the 23 PIES sites. The resulting H_{MAP} and corresponding H_{PIESLP} values achieved correlations of 0.89 with an rms difference of 3.9 cm (Figure 1.4a).

EOF analysis was applied on their residual values. EOF modes select spatially coherent patterns. Of the 23 EOF modes, the first two modes are significant. They account for 44%+18%=62% of the total energy. The third and fourth EOF modes account for only 8% and 5% of the total energy. Our purpose in this section is to illustrate two types of aliasing that cause satellite SLA errors. This purpose is served by examining just the first two EOFs.

Figures 1.4b-d and 1.4e-g show properties of the first and second modes, respectively. The physical significance of the second mode (18%) is easiest to explain because of its regular oscillation with amplitude of approximately 2.6 cm and period 95 days. It arises from aliasing of a residual M_2 tidal component by ERS-2 that has an aliasing period at 94.49 days [Morimoto et al, 2000a]. The spatial pattern of this mode agrees with that of the M_2 constituent in this region [Park et al, 2006]. The line of zero-crossing amplitude near 36.5N 130.5E is near an

amphidromic point of the M_2 tidal constituent.

The time series of the first mode (44%) exhibits broad energy at periods ranging from 30 to 370 days plus a peak at 63 days. We suggest that the first mode arises as a mixture of tidal aliasing and other aliasing detailed below: the peak at a period of 63 days is likely to arise from aliasing of a residual M_2 tidal component by T/ P with a period of 62.11 days. We will provide evidence in Section 1.5 that the broad energy at periods ranging from 30 to 370 days is likely to arise from non-tidal aliased energy (periods shorter than 70 days), which is a mixture of the common mode and other small scale variability; thus the spatial pattern appears to be a uniform background (same sign) plus some mesoscale structures. As shown in Figure 1d the T/P ground tracks provide very sparse coverage, just two tracks. Moreover, comparing their location with the M_2 tidal model [Park et al, 2006], neither tracks samples the region of higher tidal amplitude near the mouth of Korea Strait, so they will not observe the EOF2 pattern. In contrast, the ERS2 ground tracks do sample the region where M_2 has increased amplitude, so their residual alias enters different EOF modes. Because these residual aliases are from a propagating process a complex EOF analysis would have captured them better. However, finding detailed structure of the error in tidal prediction is not our purpose here, but rather simply to demonstrate that tide prediction must be improved in the JES else substantial alias error remains.

Aliasing of residual M_2 tides by T/P accounts for 16% of the first mode variance, and 44%×16%=7% of the total variance. Aliasing of residual M_2 tides by ERS-2 accounts for 90% of the second mode, and 18%×90%=16% of the total variance. ERS-2 may cause more aliased error in H_{MAP} because there are more ERS-2 ground tracks (almost 8 compared to 2 for T/P) and they sample the higher amplitude portion of M_2 (see section 1.4). In additional to tidal aliasing, the variance of

9

non-tidal aliasing accounts for 84% of the first mode variance, and 44%×84%=37% of the total variance.

1.4 Correlation Scales from Satellite Altimetry and PIES Measurements

Common mode signal and steric seasonal signal (estimated from the spatial average of baroclinic components) are both large-scale signals, which need to be removed to reveal the correlation scales of mesoscale variability. With the nearly continuous PIES measurements, the spatial correlation function can be estimated in both along-track and cross-track direction from simultaneous PIES and satellite altimeter measurements. Time correlation scales for SLA can be derived from PIES data alone.

1.4.1 Spatial Correlation Scale

Time series of simultaneous measurements from T/P, ERS-2 and PIES were used to estimate the spatial correlation scale. The correlations between the sea level of each PIES site and the sea level of T/P, ERS-2 in nearby tracks, and the other PIES sites were calculated as a function of radial distance. Figures 1.5a and 1.5b illustrate an example of the correlation estimate as a function of radial distance for PIES site P2-3, before and after removing the large-scale signals. The correlation estimates from all the PIES sites were combined and smoothed by a 15 km low-pass filter; the filtered result is shown in Figure 1.5c.

In Figure 1.5c, the spatial correlation coefficients of the total variability are generally near or above a constant 0.5, due to the existence of the large-scale signals. After the large-scale signals are removed, the spatial correlations reveal an approximately Gaussian form for the mesoscale variability. The smoothed spatial correlations of mesoscale variability were least-squares-fitted to

$$R(r) = Ae^{-(\frac{r}{r_0})^2} \tag{1.2}$$

where the spatial lag r is the horizontal distance between two locations. Parameter A is related to a signal-to-noise ratio. The fitted e-folding scale $r_\circ$ is 53 km.

1.4.2 Temporal Correlation Scale

Temporal autocorrelations are derived from each of the 23 PIES time series as a function of time lag. The average of the temporal autocorrelations is shown in Figure 1.6, before and after removing the large-scale signals. The average of the autocorrelations is modeled as a function of time lag t by an exponential function:

$$R(t) = e^{-\frac{t}{T}} \tag{1.3}$$

.

The fitted e-folding scale T for the total sea-level variability is 38 days as shown in Figure 1.6a, and the corresponding value of the mesoscale sea-level variability (after removing large scale signals) is 48 days as shown in Figure 1.6b. The removed common mode signal contributed energetic fluctutions that shorten the temporal correlation scale.

1.5 Aliasing of the Common Mode in Altimetry

1.5.1 Aliased Energy Estimated From PIES Measurements

The SLA spectra were estimated from H_{PIES} at all 23 sites in order to illustrate what fraction of variance occurs at frequencies higher than the Nyquist frequencies of T/P or ERS-2. Figure 1.7 shows the variance-preserving power spectra from 23 PIES time series before and after removing the common mode. Compared with Figure 1.7a, Figure 1.7b has lower energy at periods shorter than 70 days and much lower energy at periods shorter than 20 days. The percentage of aliased

energy may be calculated from the cumulative power spectrum shorter than the satellite Nyquist periods (20 days for T/P and 70 days for ERS-2) divided by the total energy. The average of the aliased energy as of percentage of total SLA is 15% and 24% for T/P and ERS-2 respectively; 93% of T/P aliased energy was suppressed after removing the common mode, and the corresponding value for ERS-2 is 80%. The uncorrelated alias can produce strong misleading 'meso-scale' features as illustrated in the following section.

1.5.2 Suppressing the Common Mode Alias in Altimeter Observations

To demonstrate the significant implications for future and past altimeter data interpretation, we illustrate aliasing of the common mode in AVISO SLA along-track and merged products, and we show how to suppress the alias by subtracting the sampled common mode from the along-track elevation.

Figure 1.8a shows ERS-2 track elevation during one 35-day orbit cycle in the JES. There are often large SLA disagreements among neighboring and crossing tracks. For example, SLA disagreements between tracks (T1 and T2) and where tracks cross (point C) have SLA disagreements about 15 cm. Thus a two-dimensional mapping would exhibit large "trackiness" [Stammer et al., 2000]; it is a signature similar to orbit error or improper modeling and removal of other short period effects. Furthermore, there is an extensive area of high sea surface topography (circled area) in Figure 1.8a; the same area of high topography exists in Figure 1.8b, which is the mapped SLA from the AVISO merged (T/P and ERS-2) SLA product for the same period. This area is the largest feature of sea surface topography in the merged map; thus its impact on the map interpretation is significant. The high topography is somewhat odd dynamically because such a large warm eddy rarely appears in the north region of the JES.

We sampled the common mode estimated from BP data along ERS-2 tracks

for the same period, and the result (Figure 1.8c) shows the common mode variability can reach 20cm. For example, large SLA disagreements are evident between adjacent tracks T1 and T2, and between tracks crossing at a point C. This illustrates a sampling problem for the altimeter produced by the common mode. There also exists an extensive aliased high of sea surface topography (circled area), corresponding to the high in the region shown in Figures 1.8a and 1.8b, which illustrates how the SLA merged data are affected by an alias of the common mode. Such an apparent region of high (or low) SLA arises from the combined effects of aliasing on several neighboring tracks. It is a more obstinate aliasing problem than 'trackiness' because the spatio-temporal influences can mimic mesoscale eddies, and appear in resulting synoptic maps.

The sampled common mode obtained from BP data (Figure 1.8c) was subtracted from Figure 1.8a to produce Figure 1.8d. Compared with Figure 1.8a, the improvement of Figure 1.8d is evident. For example, after subtracting the common mode, the large SLA disagreement between tracks T2 and T1 is greatly reduced; the same improvement occurs at point C; moreover, the spurious region of sea surface topography disappeared after subtracting the sampled common mode field. This exemplifies how the removal of the common mode calculated from BP measurements can significantly suppress aliasing in altimeter observations in the JES.

1.5.3 A Method to Suppress the Common Mode Alias in Other Years

Using averaged BP as representing barotropic common mode, we examine the effectiveness of using averaged sea level from hourly measured tide gauges (TG) inside the JES as an alternative proxy for the common mode, since these data are available for long durations.

All the hourly TG data were de-tided by the same procedure as BP measure-

ments. In order to reduce wind set up and coastal trapped wave effects upon the TG proxy for the common mode (Figure 1.9a), TG records from 17 sites were first individually examined and three stations were excised from the hourly average because they had obviously noisier data (not shown). The averaged and de-tided BP and TG data have little energy (1%) for periods shorter than 1.2 day. They were subsampled every 12 hours at times corresponding with the atmospheric data. We estimated the common mode time series by subtracting the local atmospheric pressure at each of the fourteen selected TG stations and averaging among them. Because aliasing error arises from sea level variability at frequencies above the satellite sampling Nyquist frequency, we focus on these higher frequencies. Figure 1.9a shows the 70-day (ERS-2 Nyquist frequency) high pass filtered common mode signal from BP and from TG. Figures 1.9b, 1.9c and 1.9d display their power spectral density, coherence and phase, respectively. The time series and the spectra agree well. Their coherence is high, with little phase difference. The fraction of BP variance captured by the TG time series is calculated by 1- $\sigma_{res}^2/\sigma_{tot}^2$, where σ_{res}^2 is the variance of the residual of the two time series, and σ_{tot}^2 is the total variance of BP sea level anomalies. The averaged sea level from TG data captures about 78% of the sea level variance from the BP. Differences between the TG and BP sea level signals could arise from at least three processes that add to the TG signals: local harbor wind setup, coastal-trapped waves, and baroclinic (steric) signals.

The effectiveness of the TG proxy for removing the common mode from altimeter data is illustrated in Figures 1.8e and 1.8f. Figure 1.8e shows the common mode estimated from TG after sub-sampling along ERS-2 tracks during the same 35-day cycle, and Figure 1.8f shows ERS-2 passes (Figure 1.8a) after subtracting Figure 1.8e. It can be seen that both the high of sea surface topography and the

trackiness are partially corrected. It indicates that the high-passed (above Nyquist frequency) TG sea level can partially (78%) correct common mode aliasing in satellite altimetric observations in the JES.

1.6 Summary and Discussion

The AVISO along-track and merged SLA products of T/P and ERS-2 are compared with SLA measurements from a two-dimensional PIES array in the JES. The overall SLA correlations between along-track T/P, ERS-2 and PIES data are 0.89 and 0.85, and corresponding rms differences are 4.7 and 5.1 cm respectively. The largest error of the merged data arises from aliasing of high frequency variability by altimetry. There are three kinds of large aliasing errors, accounting for 62% of the total error of the merged SLA product in the JES: aliasing of residual M_2 tidal component by T/P (7% of variance or 1 cm rms), aliasing of residual M_2 tidal component by ERS-2 (18% or 1.7 cm), and aliasing of the common mode (37% or 2.4 cm). The tidal alias can be reduced by an improved tide model in the JES. We propose here a method to reduce common mode aliasing.

The space and time correlation scales are 53 km and 48 days after removing large-scale variations in the JES. These observed correlations offer great promise for resolving mesoscale features in the JES by the combined spatial and temporal sampling afforded by merging T/P and ERS-2 data. But we precondition this statement with a reminder that the serious common mode alias must first be reduced in the altimeter observations.

The energetic high frequency common mode signal in the JES is shown to produce large aliasing errors in satellite altimeter observations. It accounts for 93% and 80% of non-tidal aliased SLA variance for T/P and ERS-2 respectively. The alias causes large disagreements among neighboring and crossing tracks, and leads to 'trackiness' when the data are mapped in two dimensions. Moreover, we

illustrate that it can produce false 'meso-scale' features in a synoptic map, such as false "highs" or "lows" in SLA topography that appear and relocate from one 35-day interval to the next. We demonstrate two effective ways to reduce this serious temporal alias. Accurate estimation and best removal of the common mode can be accomplished by one or a few BP gauges in the JES. A good proxy that accounts for 78% of the common mode variance is afforded by averaging the hourly TG data from 14 coastal sites in the JES (Figure 1.1), selected for low noise.

A common mode signal is likely to be found in other nearly-enclosed marginal seas [Garrett, 1983]. It will produce a substantial alias unless it can be removed. We suggest that adding BP measurements in marginal seas would be most effective for the future removal of common mode aliasing in satellite observations. We further suggest that a suitable proxy for removing much of the common mode from past altimeter records may be generated by averaging among coastal TG records. Although we focus on altimetry, results are also of interest to aliasing challenges facing gravity satellite missions, such as the Gravity Recovery and Climate Experiment (GRACE). The GRACE mission provides maps of sea floor pressure typically at intervals of 30 days. Bottom pressure signals at periods less than the chosen output interval will alias into those maps, and leak non-locally to other spherical harmonics (S. Jayne, WHOI, personal communication). A coastal TG proxy would also help reduce common mode aliasing in the GRACE measurements.

References

Byun, S.-K., C. Kim, K.-I. Chang and D. Jeon, 1997, Hydrographic characteristics observed near Ulreung Island in summer 1996, *Proceedings of the CREAMS'97 International Symposium,* Fukuoka, Japan, 89-91.

Chang, K.-I., W.J. Teague, S.J. Lyu, H.T. Perkins, D.-K. Lee, D.R. Watts, Y.B. Kim, D.A. Mitchell, C.M. Lee, and K. Kim, 2004, Circulation and currents in the southwestern East/Japan Sea: Overview and review, *Progress in Oceanography,* 61, 105-156.

Garrett, C., 1983, Variable sea level and strait flows in the Mediterranean: a theoretical study of the response to meteorological forcing, *Oceanologica Acta,* 6, 79-87.

Ducet, N., and P.Y. Le Traon, 2000, Global high-resolution mapping of ocean circulation from TOPEX/Poseidon and ERS-1 and -2, *Journal of Geophysical Research,* 105, 19477-19498.

Hendry, R.M., D.R. Watts, and C.S. Meinen, 2002, Newfoundland Basin sea-level variability from TOPEX/POSEIDON altimetry and inverted echo sounder - bottom pressure measurements, *Canadian Journal of Remote Sensing,* 28, 544-555.

Lie, H.-J., S.-K. Byun, I. Bang and C.-H. Cho, 1995, Physical structure of eddies in the southwestern East Sea, *Journal of Korean Society Oceanography,* 30, 170-183.

Lyu, S.J., and K. Kim, 2005, Subinertial to interannual transport variations in the

Korea Strait and their possible mechanism, *Journal of Geophysical Research,* 110, C12016, doi:10.1029/2004JC002651.

Mitchell, D.A., M. Wimbush, D.R. Watts, G. Sutyrin and W.J. Teague, 2004a, The Residual GEM technique and its application to the southwestern Japan/East Sea, *Journal of Atmospheric and Oceanic Technology,* 21, 1895-1909.

Mitchell, D.A., Y. Xu, K.L. Tracey, D.R . Watts, M. Wimbush, and W. J. Teague, 2004b, PIES Data Report: Ulleung Basin in the Japan/East Sea, University of Rhode Island, *Graduate School of Oceanography Technical Report,* 2004-02, 98pp.

Mitchell, D.A., W.J. Teague, M. Wimbush, D.R. Watts, and G.G. Sutyrin, 2005, The Dok Cold Eddy, *Journal of Physical Oceanography,* 35, 273-288.

Morimoto, A., T. Yanagi, and A. Kaneko, 2000a, Tide correction of altimetric data in the Japan Sea, *Journal of Oceanography,* 56, 31-41.

Morimoto, A., T. Yanagi, and A. Kaneko, 2000b, Eddy field in the Japan Sea derived from satellite altimetric data, *Journal of Oceanography,* 56, 449-462.

Munk, W.H., and D.E. Cartwright, 1966, Tidal spectroscopy and prediction, *Philosophical Transactions Royal Society London,* 259, 533-581.

Nam, S.-H., S.J. Lyu, Y.-H. Kim, K. Kim, J.-H. Park, and D.R. Watts, 2004, Correction of TOPEX/POSEIDON altimeter data for nonisostatic sea level response to atmospheric pressure in the Japan/East Sea, *Geophysical Research Letters,* 31, L02304, doi: 10.1029/2003GL018487.

Park, J.-H., and D.R. Watts, 2005, Response of the southwestern Japan/East Sea to the atmospheric pressure, *Deep-Sea Research II,* 52, 1671-1683.

Park, J.-H., D.R. Watts, K.L. Tracey, and D. A. Mitchell, 2005, A multi-index GEM technique and its application to the southwestern Japan/East Sea, *Journal of Atmospheric and Oceanic Technology,* 22, 1282-1293.

Park, J.-H., D.R. Watts, M. Wimbush, J.W. Book, K.L. Tracey and Y. Xu, 2006, Rapid variability and its links to mesoscale circulation in the Japan/East Sea: basin osciallations, internal tides, and near-inertial oscillations, *Oceanography,* 19, 48-57.

SSALTO/DUACS User Handbook, 2004, (M) SLA and (M)ADT Near-Real Time and Delayed Time Products, SALP-MU-P-EA-21065-CLS, Edition 1.2, 21-14.

Stammer, D., C. Wunsch, and R.M. Ponte, 2000, De-aliasing of global high frequency barotropic motions in altimeter observations, *Geophysical Research Letters,* 27, 1175-1178.

Teague, W.J., Z.R. Hallock, G.A. Jacobs, and J.L. Mitchell, 1995, Kuroshio sea surface height fluctuation observed simultaneously with inverted echo sounders and TOPEX/POSEIDON, *Journal of Geophysical Research,* 100, 24987-24994.

Teague, W.J., S.J. Lyu, H.T. Perkins, D.-K. Lee, D.R. Watts, Y.B. Kim, D.A. Mitchell, C.-M. Lee, and K. Kim, 2004, Circulation and currents in the southwestern East/Japan Sea: Overview and review, *Progress in Oceanography,* 61, 105-156.

Tierney, C., J. Wahr, F. Bryan, and V. Zlotnicki, 2000, Short-period oceanic circulation: Implications for satellite altimetry, *Geophysical Research Letters,* 27, 1255-1258.
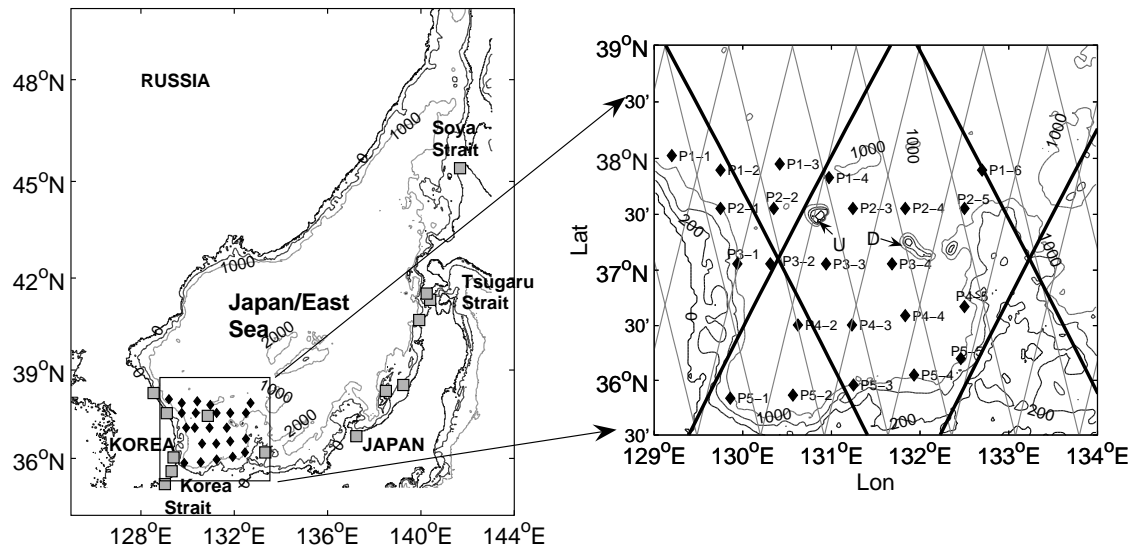
Figure 1.1. The Japan/East Sea. Small black diamonds and large gray squares respectively indicate PIESs and tide gauge stations. The PIES site identification numbers Pn-m are shown. Bathymetry contours are in meters. U:Ulleung Island. D: Dok Island. In expanded diagram on right, satellite altimeter track lines are shown for T/P (dark) and ERS-2 (light).
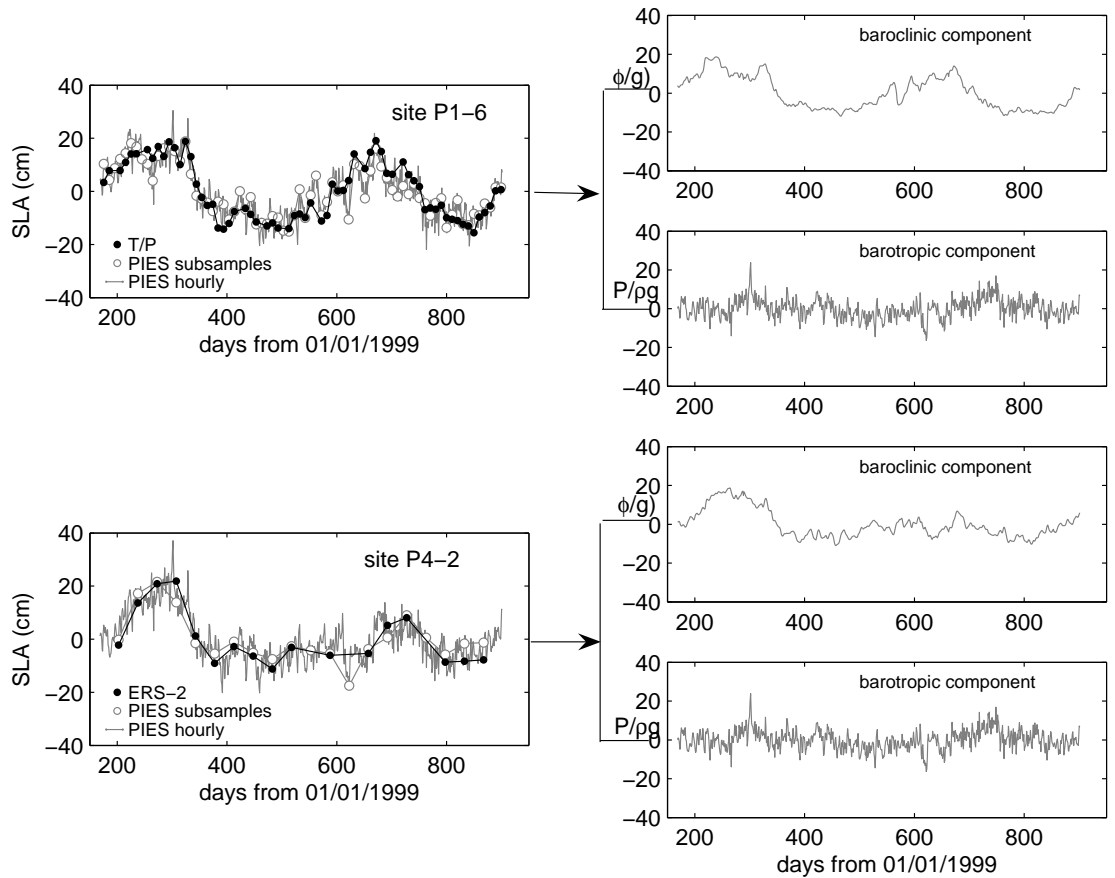
Figure 1.2. SLA from T/P, ERS-2 and PIES at sites P1-6 and P4-2. PIES hourly records are subsampled to times of respective altimeter passes. Right column shows separately barotropic and baroclinic components of SLA from PIES measurements. Time is in days from 0^h GMT 1-January-1999.
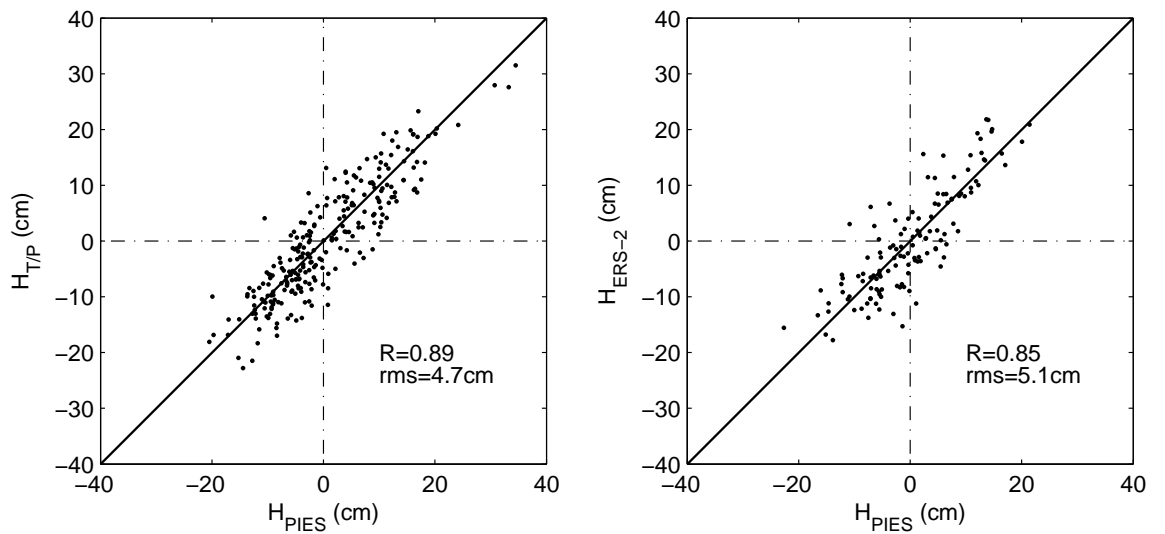
Figure 1.3. Scatterplots of SLA from PIES H_{PIES} versus SLA from T/P ($H_{T/P}$, left panel) and ERS-2 (H_{ERS-2}, right panel) for all comparisons.
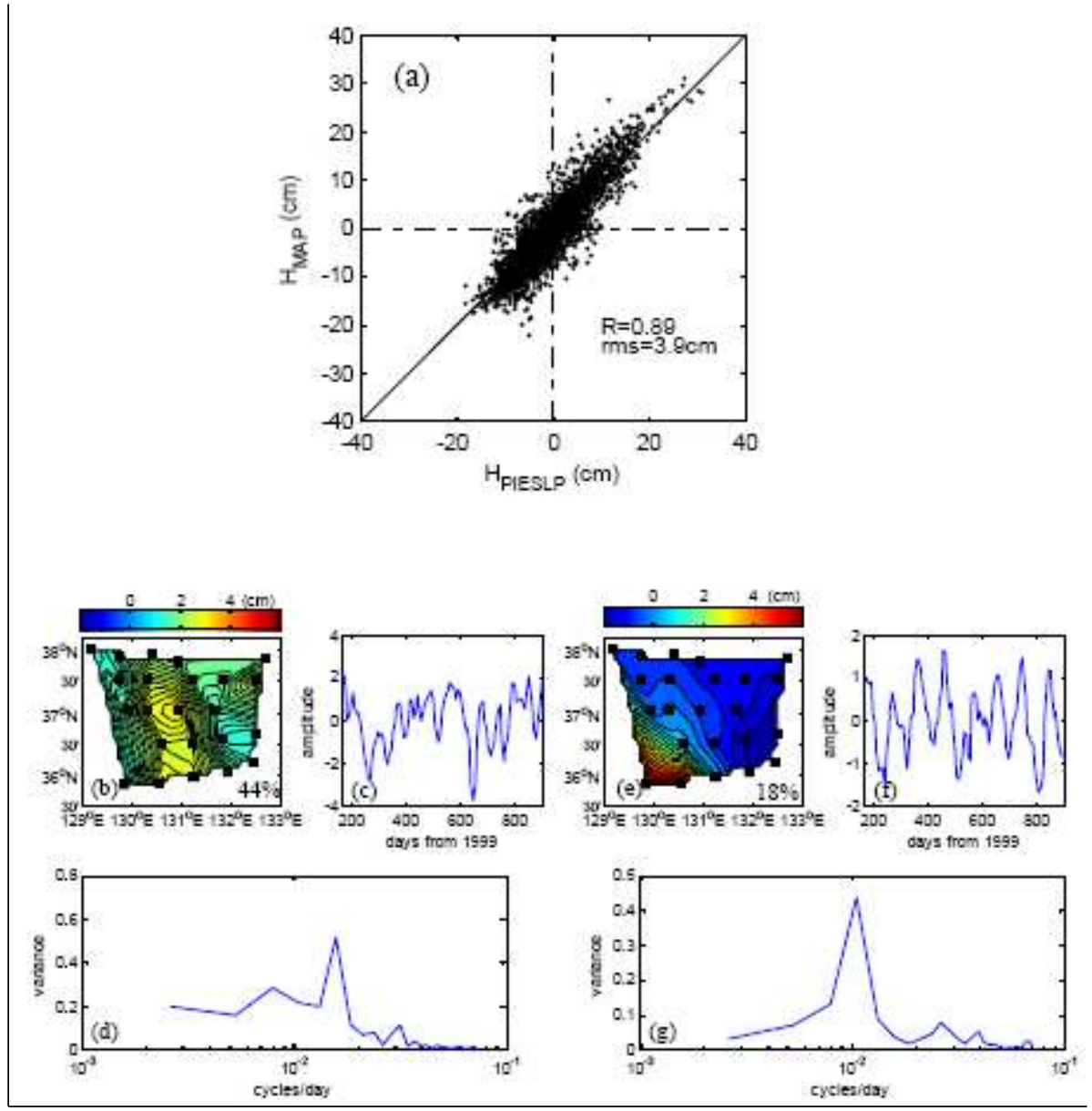
Figure 1.4. (a) Scatterplots of the coincident H_{PIESLP} versus H_{MAP}. (b)-(g) are EOFs of residuals of the coincident HPIESLP and HMAP: (b), (c) and (d) respectively show the first EOF spatial pattern, time series and variance preserving spectrum of the time series. (e), (f) and (g) show the same properties for the second EOF. The first and second EOFs account for respectively 44% and 18% of the variance.
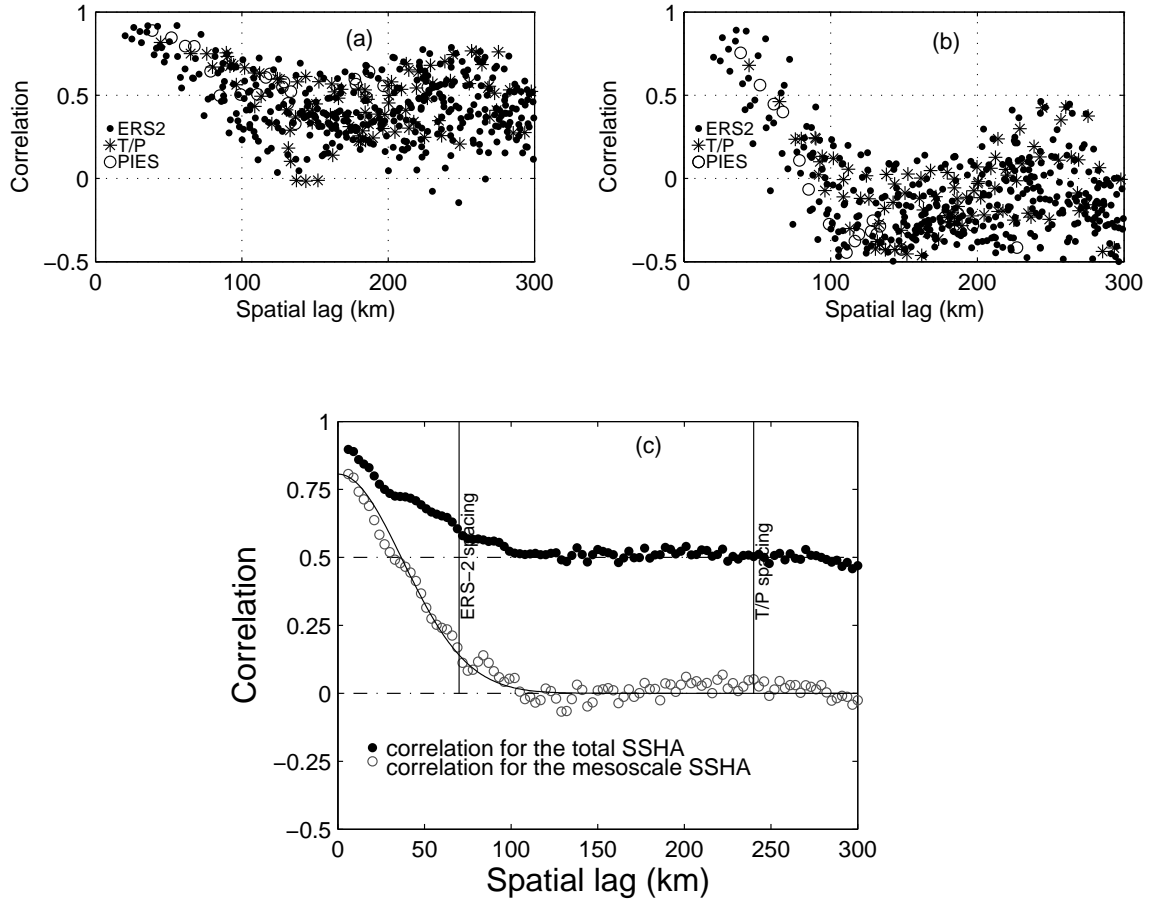
Figure 1.5. The upper panels show correlations of SLA from PIES and satellite simultaneous measurements as a function of the distance to site P2-3 before (a) and after (b) removing large scale (common mode and seasonal signal) variations. The lower panel (c) is filtered spatial correlations of all simultaneous SLA before (solid circles) and after (open circles) removing basin scale variations. Solid curve is a Gaussian correlation model as described in the text.
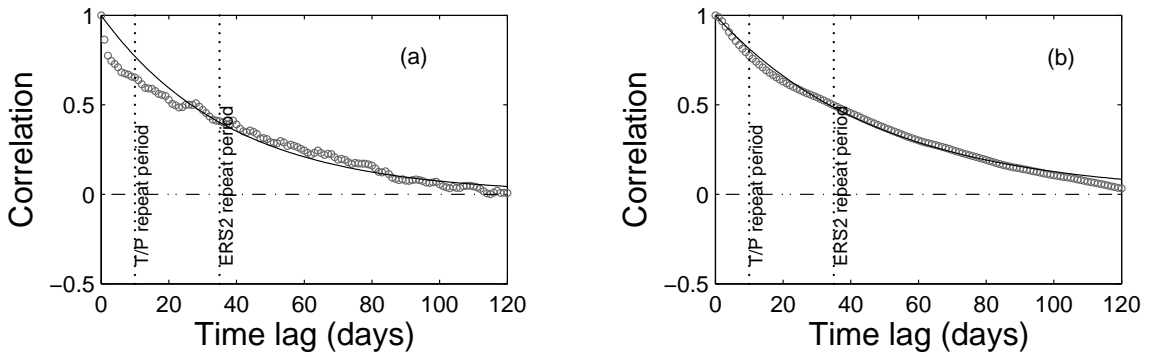
Figure 1.6. Average of the temporal autocorrelations from all 23 PIESs as a function of time lag (open circles) before (a) and after (b) removing large scale (common mode and seasonal signal) variations. Solid curve is a exponential correlation model as described in the text.
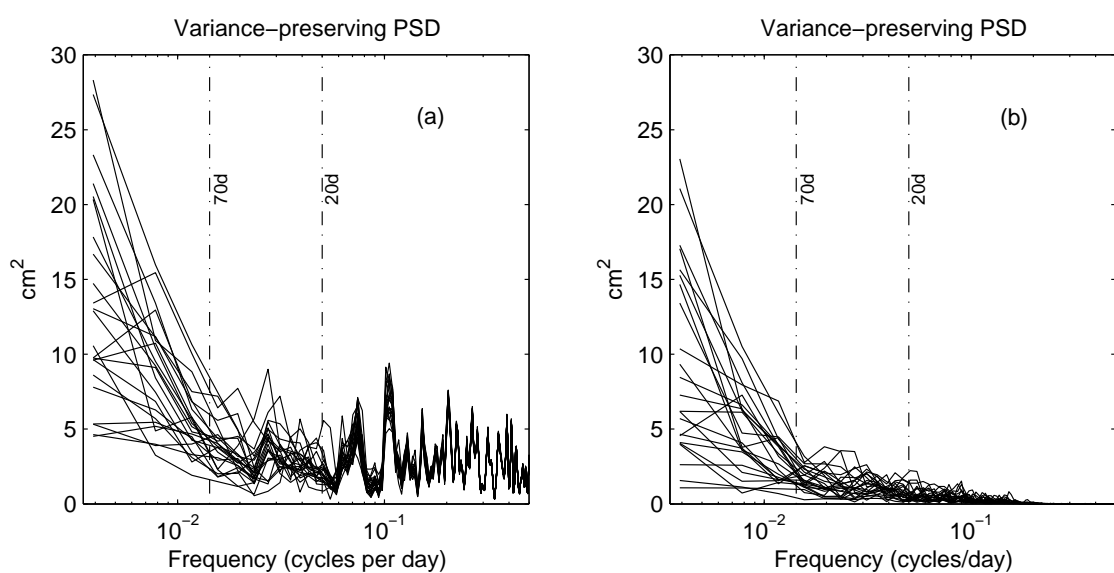
Figure 1.7. Variance−preserving power spectra of SLA from all 23 PIESs before (a) and after (b) removing the common mode.
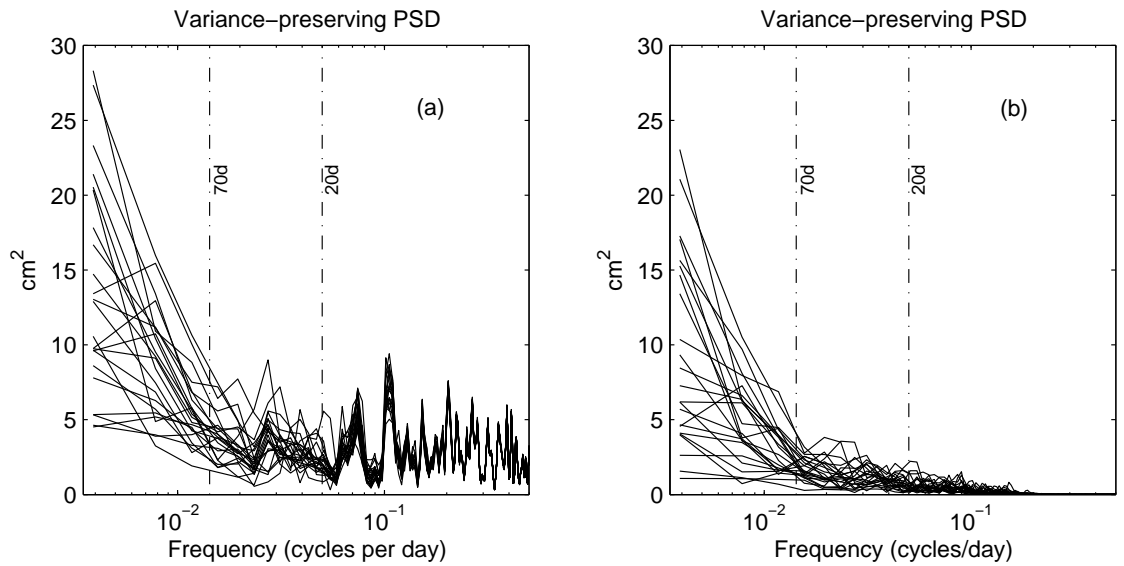
Figure 1.8. (a) ERS-2 along-track elevation for one repeat cycle (cycle 51). (b) H_{MAP} from the merged data averaged for the same period.(c) and (e) are respectively common modes from BP and TG sampled along ERS-2 tracks for the same period. (d) and (f) show the data from (a) after subtracting (c) and (e) respectively. Tracks T1, T2, point C and the highlighted area are discussed in the text. Aliasing is suppressed by removing the common modes as estimated from BP or TG data.
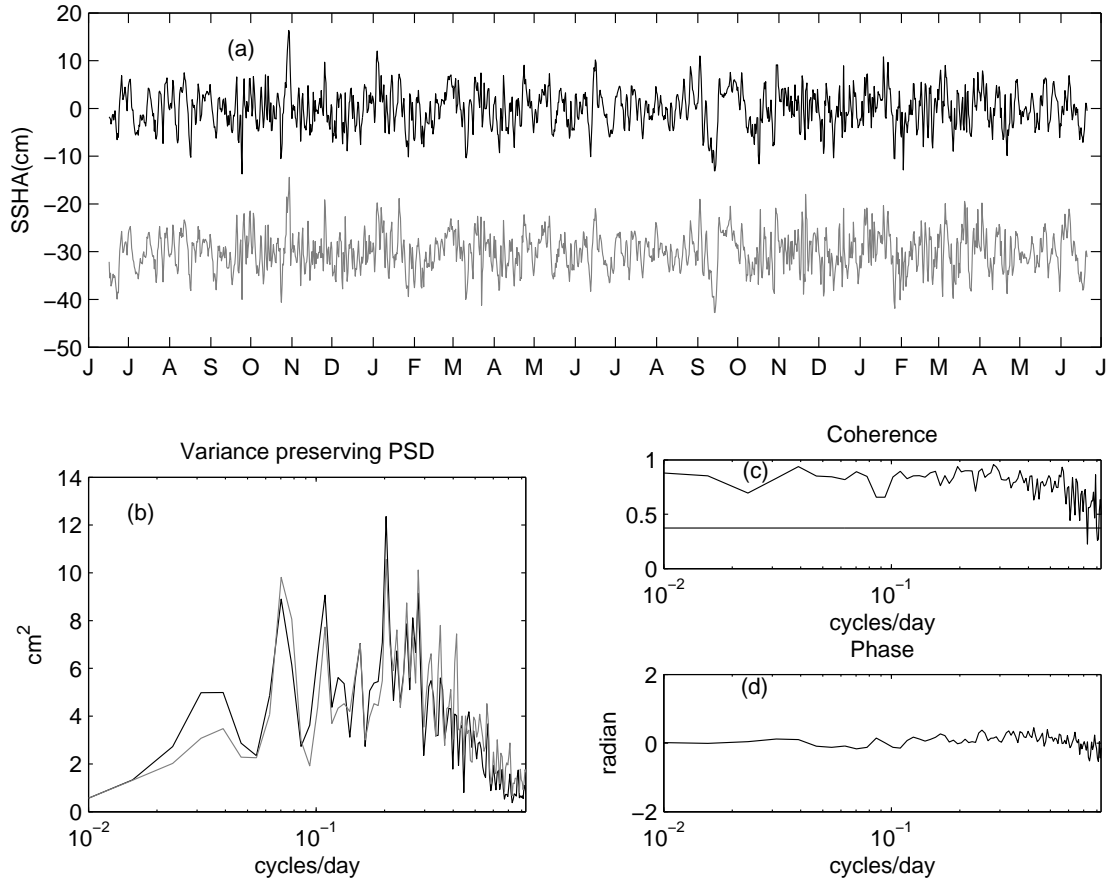
Figure 1.9. (a) 70-day high-pass filtered common modes from bottom pressure (black) and tide gauges (gray). (b), (c) and (d) are their variance preserving spectra, coherence, and the phase of coherence respectively. The horizontal thin line in (c) indicates the 95% confidence level.

MANUSCRIPT 2

Fundamental basin-mode oscillations in the Japan/East Sea

Abstract

We present observational evidence from coastal tide station and bottom pressure data that basin mode oscillations exist continually in the Japan/East Sea (JES). The fundamental basin mode is a Kelvin-wave-like oscillation consisting of a single amphidromic system around which the high water propagates counter-clockwise. Its period is about 7 hours and its coastal wavelength is equivalent to the circumference of the JES. The relative amplitudes of the observed oscillations agree with Rikiishi's model results except for stations near the Korea Strait where the closed boundary in the model produces unrealistically high amplitudes. The basin oscillation amplitudes are energetic at synoptic time scales (2-16 days). The optimal wind direction to generate basin-mode oscillations is along 60°/240°T.

2.1 Introduction

The Japan/East Sea (JES) is a semi-enclosed marginal sea, whose coastal boundary largely separates it from the open ocean. The boundary prevents energy propagating away from the basin and constrains its free oscillations to discrete modes.

Numerical studies [Platzman, 1972] have suggested that free oscillations in enclosed seas should be the normal-mode solutions for a two-dimensional basin. Observational evidence for these free oscillations in various semi-enclosed seas has come from occasional seiche episodes [Cerovecki et al., 1997; Leder and Orlic, 2004; Metzner et al., 2000]. In the JES, Rikiishi [1986] studied the basin-mode oscillations with a barotropic model assuming closed straits and flat bottom. The JES is large enough that the Earth's rotation affects the basin modes. Rikiishi's

model indicated that the fundamental basin oscillation in the JES is a Kelvin-wave-like motion around an amphidromic point with a period of 6.13 hours and a coastal wavelength equal to the circumference of the basin, as exhibited in Figure 2.1. The modeled mode has relatively large amplitudes in the narrow northern region and in the southwest corner of the JES.

In the real JES, energy dissipation exists and four straits connect to the open ocean, so Rikiishi's model may be expected to differ somewhat in period and structure from observations. We find no published report of direct observations of basin oscillations in the JES. In this paper we provide the first observational evidence that fundamental mode basin oscillations exist continually in the JES. The observed results are compared with Rikiishi's model, and the forcing is investigated.

2.2 Data and Methods

Sea level, bottom pressure, and wind stress data from the JES were analyzed. Hourly bottom pressure data came from pressure-sensor-equipped inverted echo sounders (PIESs) deployed in the southwestern JES (circles in Figure 2.1) for the period June 1999-July 2001 [Mitchell et al., 2004]. In addition, hourly sea level data at 9 tide stations were acquired from the Korea Oceanographic Data Center and the Japan Oceanographic Data Center for the period January 1999-June 2001 (squares in Figure 2.1). Fourteen tide gauge sites were available which all exhibited a consistent set of amplitudes and phases in the band of basin oscillations, and we have simply chosen to show a subset of nine which are well separated along the coast. One (15th) tide gauge inside the harbor between stations 4 and 5 was excluded because it had an inconsistent phase (by ∼5 degrees) compared to tide station 4. The NOGAPS Reanalysis Data of wind stress in the JES area were used with data interval 6 hours and grid size 1°×1°.

Three data analysis steps were performed sequentially to reveal the evidence

of basin mode oscillations in the JES. Power spectral analysis on the time series of sea level data and bottom pressure data identified the frequency band of the basin oscillation in the JES, with period between 6.42 and 7.75 hours. These 7-hour basin-mode oscillations were then isolated using a narrow band-pass filter passing frequencies between these two periods. Complex empirical orthogonal function (CEOF) analysis of the band-pass filtered data revealed the coherent basin-wide nature of these oscillations and determined their spatial structure and phase propagation.

In an effort to investigate the energy sources of the basin oscillations, we have examined the hourly Korea Strait transport, seismic activity around the JES and wind forcing. There was no significant coherence with Korea Strait transport in the basin mode frequency-band (Appendix B). We found no clear consistency between bursts of basin-mode oscillations and seismic events (Appendix C). Section 2.3 will apply cross wavelet analysis [Grinsted et al., 2004; Torrence and Compo, 1998] to characterize the joint variability of the basin oscillations and basin averaged wind stress, and investigate the influence of wind direction.

2.3 Results and Discussions

2.3.1 Evidence of basin-mode oscillations

Figure 2.2 shows power spectra for time series measurements of sea level at tide station 9 and of bottom pressure at PIES site 3, respectively in the northeastern and southwestern JES. Both sites exhibit enhanced energy (nearly ten times background level) for frequencies between the tidal peaks M_3 and M_4 (i.e., periods 6.42-7.75 hours, with peak at 6.7 hours). This non-tidal enhanced energy has a period close to that of the fundamental basin mode modeled by Rikiishi. We show below that the amplitude and phase propagation of signals in this frequency band

32

correspond to a fundamental basin mode. Moreover we checked all the peaks at periods from 2 days to 2 hours, and this is the only frequency band for which the signals exhibit consistent basin-scale propagation. Hence we identify this band with basin mode oscillations and proceed now to examine its properties in detail.

The CEOF eigenvectors represent the relative amplitudes and phases of the fluctuations [Emery and Thomson, 2001; Katz, 1997]. Figures 2.3a and 2.3b show the eigenvectors of the first CEOF, accounting respectively for 89% and 41% of the bottom pressure and sea level variances in this band. There are at least four processes that could account for the lower percentage contribution (41%) to the tide-gauge variances: local harbor wind setup, coastal-trapped waves, local baroclinic (steric) signals, and sea level response to atmospheric pressure change within this frequency band.

In Figure 2.3, CEOF eigenvectors rotate systematically through the numbered sites, corresponding to counter-clockwise phase progression in the JES along the coastal tide stations (Figure 2.3a) and PIES sites (Figure 2.3b). In Figures 2.3a, the phase rotates approximately 180 degrees from tide stations 1 to 8, and the corresponding along-coast distance is about half the basin circumference. This indicates that the coastal wavelength of the oscillation is just the circumference of the basin. The phase rotation among the PIES sites is small because the area coverage of the PIES sites is small. The phase rotation in the Rikiishi [1986] model is also small through the PIES area, yet the observed and modeled phases agree well.

In Figure 2.3a, the relative amplitudes of the first CEOF exhibit geographic variability that also resembles the Rikiishi [1986] model. Both Figure 2.3a and Figure 2.1 exhibit large amplitudes at tide station 9. The amplitudes decrease by a factor of 7 from tide station 9 to tide station 7, and then increase by a factor

33

of 2 from tide station 7 to tide station 5. For tide stations 1-4, the observed relative amplitudes are smaller than Rikiishi's model results. This is presumably an artifact of the Rikiishi model, which treats the Korea Strait as closed. In the real JES, there will be partial transmission and energy leakage through this wide strait. Hence, the closed boundary in the numerical model probably accounts for its overestimation of basin-oscillation amplitudes near the strait.

Figures 2.4a and 2.4b respectively show time series of the first CEOF from the coastal tide stations and the bottom pressure recorders. The two time series of the amplitude modulation (envelope) of the 7-hour basin-mode oscillations exhibit bursts of high variance at similar intervals of 2-16 days. These bursts have higher amplitude in the three winters than in the three summers. Figures 2.4c, 2.4d, and 2.4e exhibit their corresponding variance-preserving spectra, coherence and phase for the overlap period (June 1999-June 2001). The two time series exhibit high energy at atmospheric synoptic time scales of 2-16 days. Their mutual coherence at periods longer than 2 days is significant, with phase close to zero. All of this suggests strongly that the sea-level and bottom-pressure measurements observe the same basin mode.

2.3.2 Energy sources of basin-mode oscillations

The fundamental basin oscillations in the JES are a free mode. Their basin-wide nature allows non-local response to a variety of mechanisms that force water motions, including changes in the wind or atmospheric pressure gradient. The non-local response to multiple forcings can therefore lead to a non-steady phase relationship and incoherence with specific or local forcing processes. We found no significant coherence between hourly wind stress in the Korea Strait and basin oscillations. We next examine the joint variability of wind forcing and basin oscillations utilizing cross wavelet analysis. Cross wavelet analysis is well suited to

reveal joint variability in two processes regardless of their phase coherence.

Figure 2.5 exhibits the cross wavelet power[1] between the time series of the first tide-station-data CEOF and the basin-averaged east-west wind stress. The cross wavelet power indicates the strength of the joint variability as a function of frequency and time. Events of statistically significant common power are observed throughout the 2-16 day band, and their time dependence reflects the episodic character of the basin oscillations and the wind events. Moreover, Figure 2.5 exhibits the clear seasonal variation of enhanced common power, highest between October and April. The circled event highlights the one strongest typhoon that passed through the JES during this two year period [Park and Watts, 2005]. Sao-mai was a Super-typhoon that arrived at the Korea Strait from the south, and during September 15-16 moved nearly due north 400 km with rapid decay to end off North Korea (2000 Annual Tropical Cyclone Report on the website of the Naval Pacific Meteorology and Oceanography Center/Joint Typhoon Warning Center).

To investigate whether basin oscillation amplitudes depend on the direction of the wind stress in the JES, we calculate the cross wavelet power between the time series of the first CEOF and the wind stress in a suite of directions at 5 degree interval around the compass. Each time series was divided by its standard deviation (std) prior to convolution with the Morlet wavelet. Standard deviations are 0.00364 m and 0.0691 N/m^2 for basin oscillations and wind stress, respectively. We calculate the ratio $\frac{\sum |W_x W_y^*|}{Var_y}$, where $\sum |W_x W_y^*|$ is the sum over time and frequency of the significant cross wavelet power, and Var_y is the variance of the basin averaged wind stress in a particular direction. This ratio represents the relative effectiveness of wind stress in different directions for generating basin

---

[1]Cross wavelet power (of two time series, $x(t)$= basin mode amplitude and $y(t)$= windstress) is estimated as the complex modulus $|W_x W_y^*|$ of the product of their Morlet wavelet transforms in the frequency-time domain. The Morlet wavelet transform is the inner product of the Morlet wavelet function with the original timeseries.

oscillations. Figure 2.6 shows that wind-stress oriented near 60°T produces the largest amplitude basin oscillations, even though the wind stress itself is twice as large in the orthogonal direction along -30°T (or 330°T). The direction 60°T is turned somewhat clockwise from the major axis of the JES (~30°T) along which wind stress would act with greatest fetch. We speculate that the turning arises from a combination of two atmospheric forcing processes that can affect sea level difference from the southern to northern end of the JES: the above noted wind stress and the atmospheric pressure difference. Zonal winds are associated with meridional atmospheric pressure gradients, which would add to the sea-level set up that is directly forced by wind stress. Consequently, a response to meridional atmospheric pressure gradient may account for the turning from the longest fetch direction (30°T) into the observed optimal direction (60°T). Because the wind and atmospheric pressure are highly correlated, their effects are not easily distinguished statistically. We suggest that a future numerical model study might consider the wind stress and atmospheric pressure forcing separately in the JES.

2.4 Conclusion

We present the first observational evidence that basin oscillations exist continually in the JES. The fundamental-mode basin oscillation, influenced by the Earth's rotation, consists of a single amphidromic point around which the wave propagates counter-clockwise. It has a period of about 7 hours and a coastal wavelength equal to the circumference of the JES.

Both tide-station and bottom-pressure data confirm counterclockwise phase rotation in the frequency band of the fundamental basin mode in the JES. The relative amplitudes support the spatial structure of the Rikiishi model, except at stations near the Korea Strait where the model assumed a closed boundary and hence obtained artificially large amplitudes.

The observed basin oscillations have amplitudes that vary on synoptic time scales (2-16 days) and exhibit both seasonal and interannual variations. The observed optimal direction of wind stress to generate basin mode oscillation is along 60°/240°T, which we attribute to the geographic shape of the JES.

The amplitudes of basin oscillations are the product of spatial amplitudes and the time component. The amplitudes of basin oscillations can reach 2-3 cm for tide station 9 and 0.2-0.4 cm for other tide stations in the JES. These high frequency signals will cause aliasing errors in the satellite observations, especially for the north narrow region. In the future, the aliasing effects arising from the basin-mode oscillations could be investigated and removed from satellite data using tide station or bottom pressure measurements.

References

Cerovecki, I,M. Orlic and M.C. Hendershott, 1997, Adriatic seiche decay and energy loss to the Mediterranean, *Deep-Sea Research I,* 44, 2007-2029.

Emery, W.J., and R.E. Thomson, 2001, Data analysis methods in physical oceanography, 2nd Edition, *Elsevier Science Inc.,* 638 pp.

Grinsted, A., J.C. Moore, and S. Jevrejeva, 2004, Application of the cross wavelet transform and wavelet coherence to geophysical time series, *Nonlinear Processes in Geophysics,* 11, 561-566.

Leder, N., and M. Orlic, 2004, Fundamental Adriatic seiche recorded by current meters, *Annales Geophysicae,* 22, 1449-1464.

Katz, E. J., 1997, Waves along the equator in the Atlantic, *Journal of Physical Oceanography,* 27, 2536- 2544.

Metzner, M., M. Gade, I. Hennings, and A. B. Rabinovich, 2000, The observation of seiches in the Baltic Sea using a multi data set of water level, *Journal of Marine Systems,* 24, 67-84.

Mitchell, D.A., Y. Xu, K.L. Tracey, D.R. Watts, M. Wimbush, and W. Teague, 2004, PIES Data Report: Ulleung Basin in the Japan/East Sea. *University of Rhode Island,* Graduate School of Oceanography Technical Report 2004-02, 98pp.

Park, J.-H., and D.R. Watts, 2005, Response of the southwestern Japan/East Sea to the atmospheric pressure, *Deep-Sea Research II,* 52, 1671-1683.

Platzman, G.W., 1972, Two-dimensional free oscillations in natural basins. *Journal of Physical Oceanography,* 2, 117138.

Rikiishi, K., 1986, Tides and natural oscillations in the Japan Sea, *Kaiyo Monthly,* 18, 447-445 (in Japanese).

Torrence, C. and G.P. Compo, 1998, A practical guide to wavelet analysis, *Bulletin of the American Meteorological Society,* 79, 61-78.
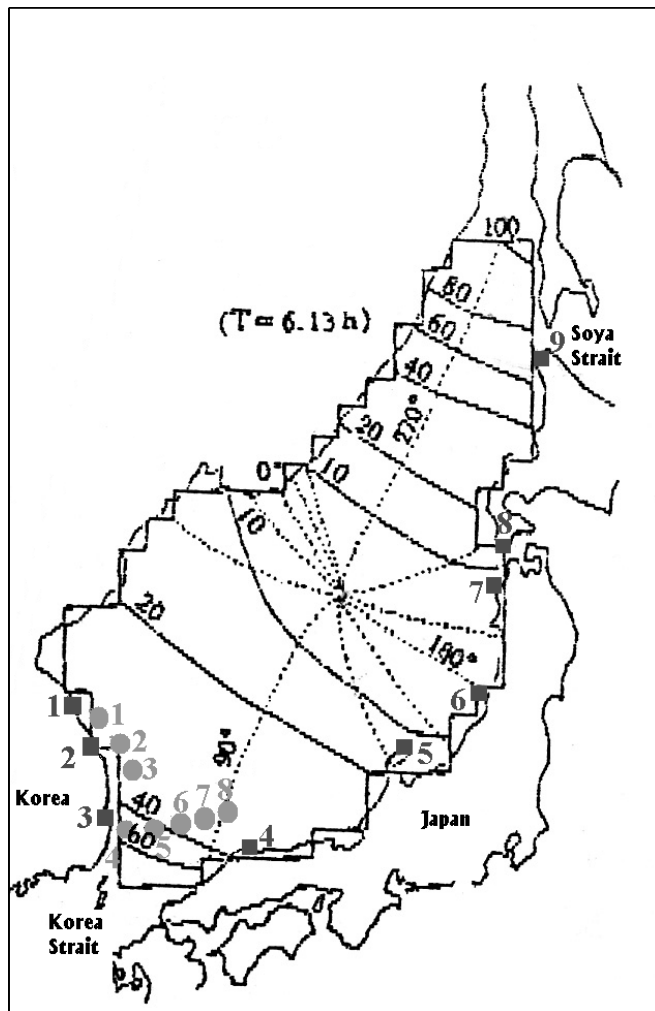
Figure 2.1. Fundamental-mode basin oscillation in the Japan/East Sea taken from the Rikiishi [1986] model. Solid lines and broken lines indicate respectively the surface elevation and phase of the fundamental-mode oscillation. Also shown are tide gauge stations (squares) and PIES sites (circles).
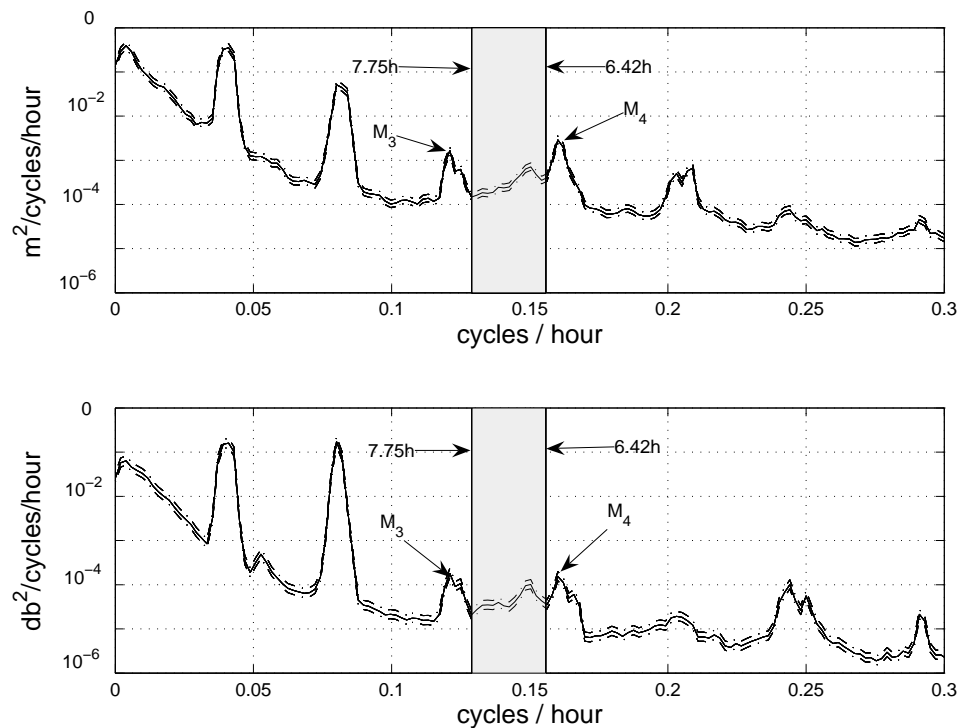
Figure 2.2. Power density spectra of sea level at tide station 9 (upper panel), and bottom pressure at PIES site 3 (lower panel). In the highlighted frequency band of fundamental basin oscillations, the power level is nearly a factor of ten higher than the background between neighboring tidal-harmonics peaks M_3 and M_4. Dashed lines indicate the 95% confidence intervals.
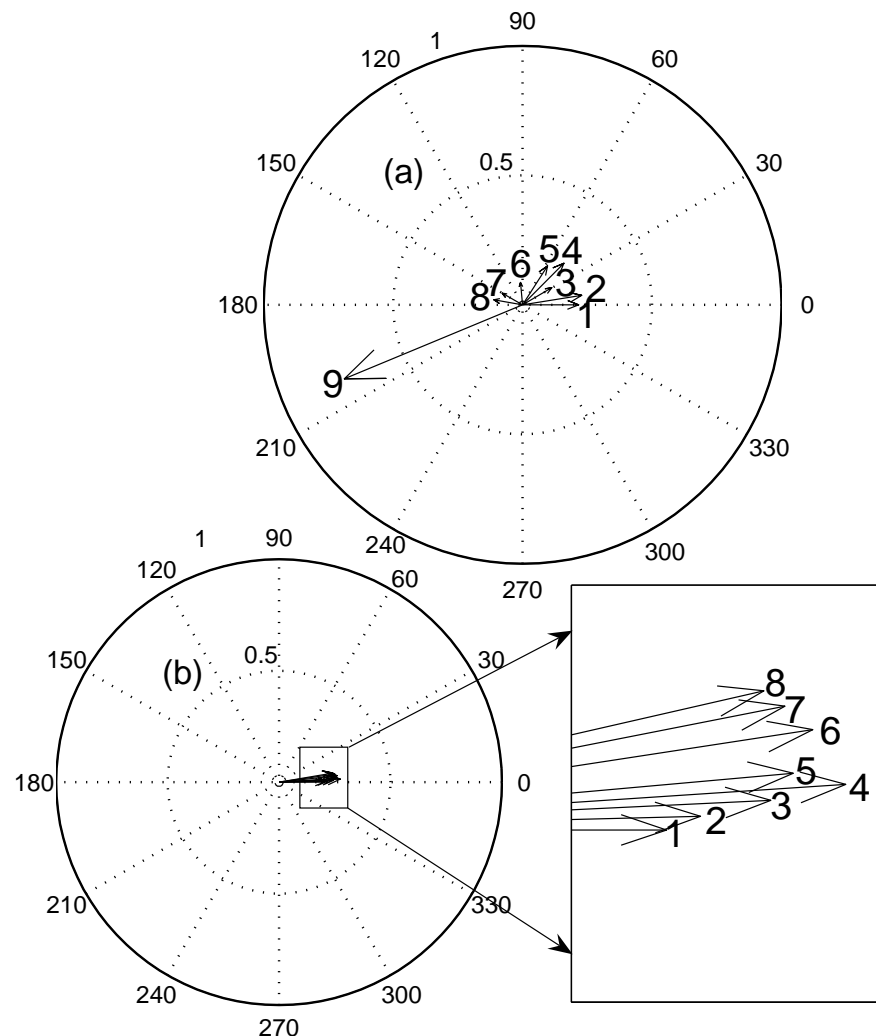
Figure 2.3. Amplitudes and phase progression of the fundamental basin oscillations indicated by eigenvectors from the first CEOF of the band-pass filtered data (6.42-7.75 hours). Vector direction and length represent respectively the relative phase lag and the amplitude. (a) and (b) correspond respectively to tide stations and PIES sites, and account for 41% and 89% of their respective variances in the 6.42-7.75 hour band. The dimensional amplitude (mm) of the envelop of basin oscillations at a given time and location is the product of the above non-dimensional vector magnitude and the time series amplitude in Figure 2.4.

42
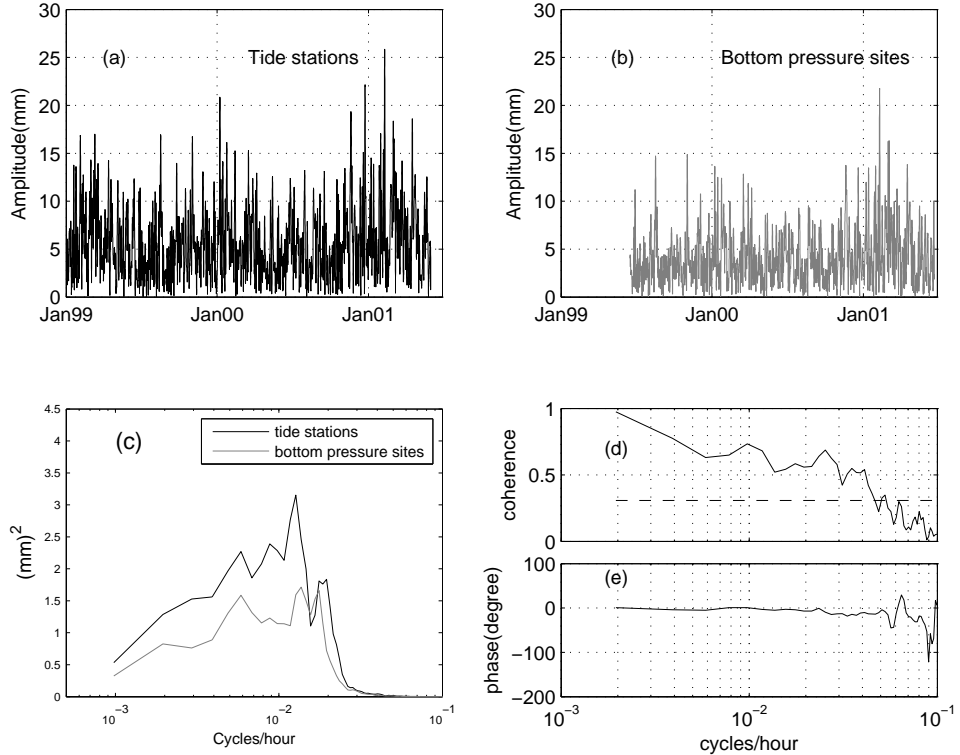
Figure 2.4. Temporal variability of the amplitude modulation of basin oscillations is consistently measured by tide stations and bottom pressure sites, and the greatest variances occur at frequencies 0.02-0.0025 cycles/hour, i.e., periods 2-16 days. Time series of the first CEOF mode of (a) tide station data, and (b) bottom pressure data, band-pass filtered between 6.42 and 7.75 hours. (c) Variance preserving spectra of (a) and (b). (d) Coherence and (e) phase of (a) and (b). The horizontal dashed line in (d) indicates the 95% confidence level of coherence. The dimensional amplitude (mm) of the envelop of basin oscillations is given by the product of these time series and the non-dimensional vector magnitude amplitude in Figure 2.3 for a given site.

43
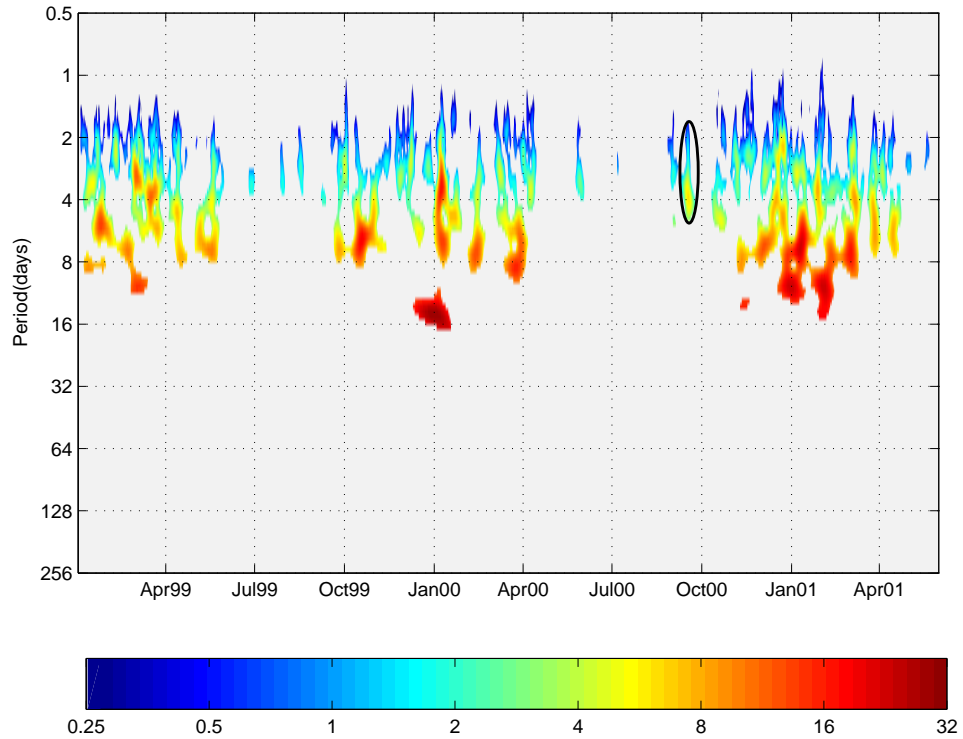
Figure 2.5. Basin oscillations and wind stress vary jointly at periods 2-16 days. Their joint variability is indicated by the cross wavelet power of the time series of the first CEOF of tide station data and the basin averaged east-west wind stress. To restore dimensional units, the values in the colorbar should be multiplied by the standard deviations, 0.00364 m and 0.0691 N/m^2 for basin oscillations and wind stress, respectively. For example, the value 8 in the colorbar corresponds to 0.00364*0.069*8=0.02 N/m. Only the values above 95% confidence level are shown. The circled spot corresponds to the passing of Typhoon Saomai across the Japan/East Sea on September 15-16, 2000.
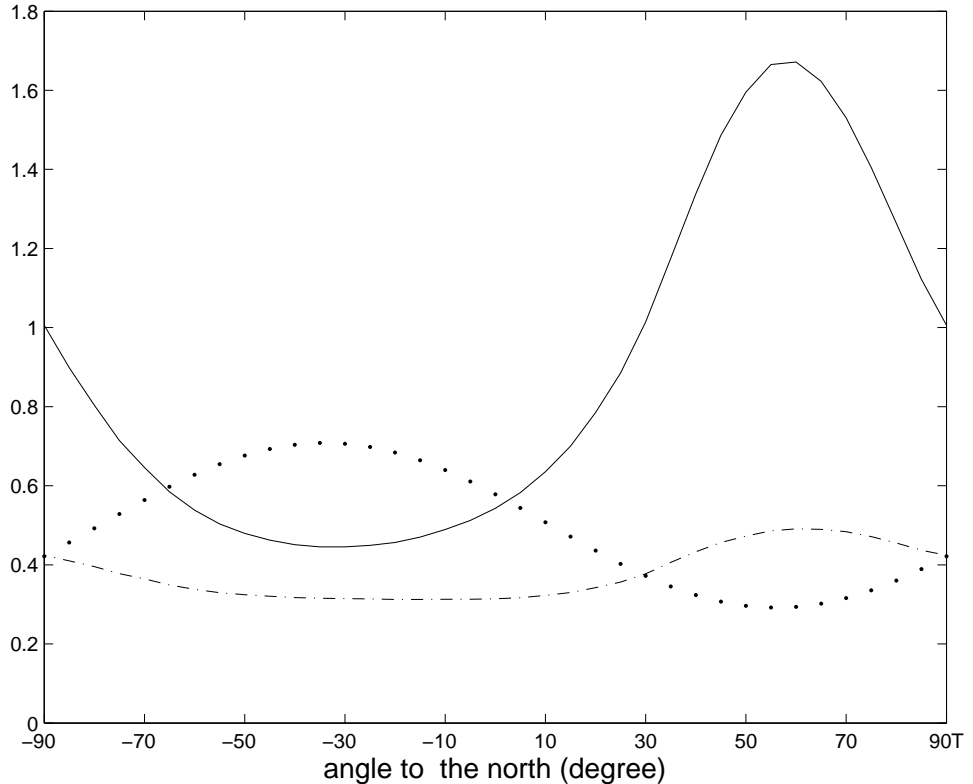
Figure 2.6. The wind stress at 60°T is most effective at generating basin oscilla-tions. The effectiveness of wind stress to generate basin oscillations (solid line) is indicated by the ratio $\frac{\sum |W_x W_y^*|}{Var_y}$. Dashed line ($\sum |W_x W_y^*|$) is the sum of the sig-nificant cross wavelet power between the time series of basin mode amplitude $x(t)$ and the wind stress $y(t)$ in a particular direction, normalized by the total time-frequency area of significant cross wavelet power (e.g., for 90°T the colored area in Figure 2.5). Dotted line (Var_y) is the basin averaged wind stress in a particular direction normalized by the variance of the total wind stress.

MANUSCRIPT 3

Coupled pattern analysis of dynamic height and bottom pressure fields in the southwestern Japan/East Sea

Abstract

Physical coupling between the shallow and deep mesoscale eddy processes in the southwestern Japan/East Sea are examined using acoustic travel-time and pressure measurements from an array of pressure-gauge-equipped inverted echo sounders moored from June 1999 to July 2001. In the first coupled mode, the upper layer exhibits a migration of the Ulleung Warm Eddy and downstream propagation of a meander trough of the Subpolar Front (SF), while the deep flows are expressed along closed potential vorticity contours created by the Ulleung Basin depression and the Korea Plateau. In the second coupled mode, the upper and deep layer have similar spatial patterns peaked at a site along the southwestern edge of the Korea plateau. The second mode appears to arise from time varying strength of a mean deep anticyclone, which had been revealed by intermediate float data, flowing around the contour of the Korea Plateau.

3.1 Introduction

The Japan/East Sea (JES) is a semi-enclosed deep marginal sea of the northwestern Pacific surrounded by Korea, Japan, and Russia. The Ulleung Basin (UB) in the southwestern JES is characterized by a central depression deeper than 2000 m, and peripheral irregular topography. The Korea Plateau (KP), located at the northern edge of the UB, is shallower than 1500 m. The anticyclonic Ulleung Eddy is perhaps the best-known eddy feature in the southwestern JES. The Subpolar Front (SF), a thermal boundary between warm southern and cold subarctic water, begins in the northwestern corner of the Ulleung Basin. The bottom water

within the Ulleung Basin, which enters through the Ulleung Interplain Gap from the northeast, circulates cyclonically. As part of this cyclonic circulation, the deep flow along the steep shelf off Korea is strongly to the south [Teague et al, 2005; Xu et al, 2003]. The coupling of upper and deep circulation has not been clarified yet.

Understanding the vertical coupling in the ocean could contribute to understanding both abyssal circulation and mixing and upper layer dynamical events. A primary scientific result of the Synoptic Ocean Prediction experiment (SYNOP) was vivid evidence of coupling between the Gulf Stream and the underlying water column near 68°W. The spin-up of the deep flow field occurred during the passage of steep meander crests and troughs of the Gulf Stream [Watts et al, 2001]. The formation of a deep eddy beneath a moving upper eddy was analyzed in a number of numerical model studies [Cushman-Roisin et al, 1990; Frolov et al, 2004; Indest, 1992; Sutyrin et al, 2003; Sturges et al. 1993; Welsh and Inoue, 2000]. Numerical model studies also suggest topography that results in regions of closed potential vorticity contours is particularly influential upon the deep ocean response [Hallberg, 1997; Thompson, 1995]. Furthermore, bottom topography can steer upper ocean currents and regulate the strength and location of flow instabilities [Hogan and Hurlburt, 2000].

Circulation and currents in the southwestern JES have been extensively investigated from measurements made in the past decade [Chang et al, 2004]. As part of the United States Office of Naval Research JES program, an array of pressure-gauge-equipped inverted echo sounders (PIESs, Figure 3.1) was deployed in the southwestern JES for two years, from June 1999 to July 2001. The PIES recorded vertical acoustic travel time and pressure hourly, from which upper and deep geostrophic stream functions were mapped daily. Mitchell et al, [2005] re-

ported five quasi-stable upper flow patterns based on four features that recur and persist in various time intervals: the East Korean Warm Current, the Ulleung Warm Eddy, the Offshore Branch, and a newly described Dok Cold Eddy. Although large-amplitude meanders and vigorous mesoscale variability are present in the southwestern JES, the vertical coupling is still difficult to observe because the bottom topography causes O(1) changes in thickness (potential vorticity) of the deep layer and produces subregions of closed PV contours. The deep flow tends to be trapped in regions of closed potential vorticity (PV) contours as a free mode [Hallberg, 1997]. Forcing on any part of the closed contour region can excite this free mode. Thus the resulting deep response to vertical coupling is not localized and is therefore subtler to observe than a local response.

The daily maps of upper and deep layer stream functions do not exhibit clearly the subtle vertical coupling. In this study, canonical correlation analysis is used to reveal the coupled modes between the dynamic height and bottom pressure fields in order to understand the physical coupling in the southwestern JES.

3.2   Data and Methods

Twenty-five PIESs were deployed with 55-60 km spacing to cover the southwestern Japan/East Sea as shown in Figure 3.1. The PIES is an ocean bottom moored instrument that measures hourly bottom pressure and the round-trip time τ for an acoustic pulse to travel from the sea floor to sea surface. Maps of τ and pressure will be interpreted in this paper as stream functions for the upper and deep flow, respectively. One PIES at P4-1 was lost, and P1-5 measured acoustic travel time for only two months. Thus, we use 23 data sets of τ and 24 data sets of pressure in this study. τ is an integral quantity that depends on the sound-speed profile of the water column. Minus τ, hereafter simply refered to as tau, can be regarded as a good proxy for steric height anomaly. The resulting 24 pressure

records were remarkably similar to one another on all time scales, with correlations between all pairs of records exceeding 0.95. This basin-wide pressure signal [Park and Watts, 2006], independent of location, is dynamically unimportant for mesoscale variability and was subtracted from all pressure records. Five-day low-pass filtering was applied to both tau and pressure records to focus on geostrophic signals. Then, the records were subsampled daily from 18 June 1999 to 20 June 2001.

Canonical correlation analysis (CCA) was applied to identify the most highly related patterns of tau and pressure variability. Appendix D discusses the derivation of canonical correlations. We followed the procedure recommended by Barnett and Preisendorfer [1987] and Bretherton et al [1992] to pre-filter the bottom pressure data by retaining only its first two leading empirical orthogonal functions (as explained in Appendix E). Since the waters in the JES below 500 dbar are nearly homogeneous and all PIESs were at pressure levels deeper than 500 dbar, the measured tau values were readily converted to tau at 500 dbar. For more detail about this conversion procedure see Mitchell et al [2004].

To test the robustness of the CCA patterns, we also calculated the integral time scale of the bottom pressure data, which we found to be approximately eighteen days. The bottom pressure and tau data were then eighteen-day low-pass filtered and subsampled at nine days, the Nyquist sampling interval. The CCA modes for the differently sampled data retain similar patterns to the 5-day low-pass filtered daily data (see Appendix F). Probability values of the chi-squared test statistic [Jobson, 1992] remain smaller than 0.05 that these modes could occur from random data. The subsampling and the chi-squared test statistic suggest the CCA modes are robust.

3.3 Results and Discussions

The first canonical correlation mode (CCA1) is shown in Figure 3.2. The CCA1 map of tau exhibits a positive anomaly in the northeast and southwest quadrants, and a negative anomaly in the northwest quadrant. When added to the time mean tau field, varying amplitudes of this standing pattern can represent a moving eddy event. This is illustrated in Figure 3.3, which reveals the dynamics associated with the CCA1 map of tau. Figure 3.3 exhibits clearly an UB warm eddy migration and development event. The UB warm eddy changes shape from an ellipse to an approximate circle while moving to the north from map-1 to map-3, and then deepens its central thermocline while it continues to the north from map-3 to map-5. At the same time, the SF meander trough shifts downstream from the northwest quadrant to the northeast quadrant, and the southwestward intrusion of cold water severs the southern connection of the UB warm eddy. The tau temporal component of CCA1 (Figure 3.2c) exhibits a feature related to the upper layer eddy activity which is linked to the Korea Strait (KS) transport, with a larger oscillation occuring during the first year. For example, CCA1 exhibits a large UB warm eddy northward migration event coinciding with a decrease in the KS transport which dropped from maximum to minimum during October 1999 to January 2000 as reported by Teague et al [2002].

The CCA1 bottom pressure field Figure 3.2b exhibits two major circulations with opposite directions, corresponding to the PV contours created by the UB Depression and the Korea Plateau, respectively. The UB Depression and the Korea Plateau are the two principal topographic features in the southwestern JES which produce strongly sloping bottom topography. It is difficult for deep flow to cross f/h contours, and it tends to follow closed PV contours of a bottom depression or rise [Hogan and Hurlburt, 2000]. The CCA1 bottom pressure map exhibits a

closed circulation around the UB Depression that is related statistically to the migration of the UB warm eddy. The sense and magnitude of change suggest the following dynamical basis for this statistical coupling. Vortex compression ($\frac{\Delta h}{H_\circ} \sim -0.01$, where Δh is themocline depth change ~ 20 m and $H_\circ$ is water depth ~ 2000 m) associated with the northward migration of the UB warm eddy would generate negative vorticity ($\frac{\zeta}{f} \sim \frac{-\Delta p}{\rho L^2 f^2} \sim -0.01$, where Δp is the pressure difference ~ 0.012 dbar and L is corresponding length scale ~ 50 km) in the deep layer. The deep eddy feature in the central northern edge of CCA1 is located along the southwestern edge of the Korea Plateau and is likely related to the downstream propagation of the SF meander trough. Vortex stretching associated with the downstream shift of the SF meander trough could account for the generation of positive vorticity in the deep layer.

The UB warm eddy is the largest eddy feature in the southwestern JES. In CCA1, the UB eddy movement spatially matches the UB Depression, and as was just shown the sign and magnitude of vortex stretching (compression) associated with the moving UB eddy agrees approximately with the deep PV change. Generation of deep eddies by vortex stretching of upper moving baroclinic structures supports the more general numerical results regarding deep eddy formation cited in Section 3.1.

In the CCA2 mode (Figure 3.4), the spatial patterns of tau and pressure are similar. Both have a spatial pattern peaked at a site near the southwestern edge of the Korea plateau (site P1-4), and up to 5 surrounding sites contribute to this extremum. The time components of CCA2 exhibit a wide range of time scales with no apparent seasonal variations.

Figure 3.5 shows the intermediate circulation from float data at about 700 m. The float data reveal an anticyclonic mean circulation around the Korea Plateau,

with relatively energetic variance ellipses also tending to encircle this region. The anticyclonic circulation observed from float data at this intermediate level would extend to the bottom because of the nearly uniform density below 700 m. P1-4 is located along the southwestern edge of the Korea Plateau, and the variability of the pressure field at P1-4 is likely to arise from the variation of the deep anticyclonic circulation around the Korea Plateau. The CCA2 map of tau indicates a corresponding variability in the upper layer. Moreover, the deep anticyclone is underneath the region where the mean SF meander trough begins (Figure 3.3 panel 3). Mitchell et al [2005] reported that the SF meander trough had developed repeatedly during the two-year period. It is possible that these variations in abyssal circulation play a role in triggering the upper layer instability, and may contribute to the formation of the SF meander trough.

3.4 Conclusion

This work investigates the coupled patterns of shallow and deep mesoscale eddies utilizing the data set from a PIES array in the southwestern Japan/East Sea. The first coupled mode supports the suggestion by Hallberg [1997] that bottom topography can have a profound influence on the deep flows if it creates regions of closed PV contours. The observed deep circulations are trapped in the closed contour region created by the UB Depression and the Korea Plateau. In the southwestern JES, the deep flows vary jointly with the migration of the UB warm eddy and the downstream shift of the SF meander trough.

Another interesting finding of this study is the relationship between the deep anticyclonic recirculation around the Korea Plateau and the mean pathway of the SF meander trough. In addition to the evidence of the anticyclonic recirculation around Korea Plateau revealed by float data in the intermediate level [Park, 2004], the CCA2 mode suggests that this anticyclone extends throughout the upper and

deep layers. The anticyclone may play an important role in triggering the upper layer meander trough formation.

References

Barnett T.P., and R.W. Preisendorfer, 1987, Origins and levels of monthly and seasonal forecasts skill for United States surface air temperature determined by canonical correlation analysis, *Monthly Weather Review,* 115, 1825-1850.

Bretherton, C.S., C. Smith, and J.M. Wallace, 1992, An intercomparision of methods for finding coupled patterns in climate data, *Journal of Climate,* 5, 541-560.

Chang, K.-I., W.J. Teague, S.J. Lyu, H.T. Perkins, D.-K. Lee, D. R . Watts, Y.-B. Kim, D.A. Mitchell, C.-M. Lee, and K. Kim, 2004, Circulation and currents in the southwestern East/Japan Sea: Overview and review, *Progress in Oceanography,* 61, 105-156.

Cushman-Roisin, B., E.P. Chassignet, and B. Tang, 1990, Westward motion of mesoscale eddies, *Journal of Physical Oceanography,* 20, 758-768.

Frolov, S.A., G.G. Sutyrin, G.D. Rowe, and L.M. Rothstein, 2004, Loop Current Eddy Interaction with the Western Boundary in the Gulf of Mexico, *Journal of Physical Oceanography,* 34, 2223-2237.

Gittins, R., 1985, Canonical analysis, *Berlin Heidelberg: Springer-Verlag,* 351pp.

Hallberg, R., 1997, Localized coupling between surface- and bottom-intensified flow over topography, *Journal of Physical Oceanography,* 27, 977-999.

Hogan, P.J. and H.E. Hurlburt, 2000, Impact of upper ocean-topography coupling and isopycnal outcropping in Japan/East Sea models with 1/8° to 1/64° resolution,

Journal of Physical Oceanography, 30, 2535-2561.

Hurlburt, H.E., 1986, Dynamic transfer of simulated altimeter data into subsurface information by a numerical ocean model, *Journal Geophysical Research,* 91, 2372-2400.

Indest, A.W., 1992, Ring dynamics in the western Gulf of Mexico, Ph.D. dissertation, *Old Dominion University,* Norfolk, Virginia, 127pp.

Jobson, J.D., 1992, Applied multivariate data analysis, *New York: Springer-Verlag,* 731pp.

Mitchell, D.A., M. Wimbush, D. R. Watts, G. Sutyrin and W. J. Teague, 2004, The Residual GEM technique and its application to the southwestern Japan/East Sea, *Journal of Atmospheric and Oceanic Technology,* 21, 1895-1909.

Mitchell, D.A., J.W. Book, K.-I. Chang, M.-S. Suk, W.J. Teague, K. L. Tracey, D.R. Watts, M. Wimbush and J.-H. Yoon, 2005, Upper circulation patterns in the southwestern Japan/East Sea, *Deep-Sea Research II,* 52, 1617-1638.

Mitchell, D. A., W. J. Teague, M. Wimbush, D. R . Watts, and G. G. Sutyrin, 2005, The Dok Cold Eddy, *Journal of Physical Oceanography,* 35, 273-288.

Park, Y.-G., K.-H. Oh, K.-I. Chang, and M.-S. Suk, 2004, Intermediate level circulation of the southwestern part of the East/Japan Sea estimated from autonomous isobaric profiling floats, *Geophysical Research Letters,* 31, L13213, doi:10.1029/2004GL020424.

Park, J.-H., and D.R. Watts, 2005, Response of the southwestern Japan/East Sea to the atmospheric pressure, *Deep-Sea Research II,* 52, 1671-1683.

Sturges, W., J. Evans, S. Welsh, and W. Holland, 1993, Separation of warm-core in the Gulf of Mexico, *Journal of Physical Oceanography,* 23, 250-268.

Sutyrin, G., G. Rowe, L. Rothstein, and I. Ginis, 2003, Baroclinic eddy interactions with continental slopes and shelves, *Journal of Physical Oceanography,* 33, 283-291.

Teague, W. J., G. A. Jacobs, H. T. Perkins, J. W. Book, K.-I. Chang, and M.-S. Suk, 2002, Low frequency current observations in the Korea Strait, *Journal of Physical Oceanography,* 32, 1621-1641.

Teague, W.J., K.L. Tracey, D.R. Watts, J.W. Book, K.-I. Chang, P.J. Hogan, D.A. Mitchell, M.-S. Suk, M. Wimbush and J.-H. Yoon, 2005, Observed deep circulation in the Ulleung Basin, *Deep-Sea Research II,* 52, 1802-1826.

Thompson, L., 1995, The effect of continental rises on the wind driven ocean circulation, *Journal of Physical Oceanography,* 25, 1296-1316.

Watts, D.R., X. Qian, and K.L. Tracey, 2001, Mapping abyssal current and pressure fields under the meandering Gulf Stream, *Journal of Atmospheric and Oceanic Technology,* 18, 1052-1067.

Welsh, S., and M. Inoue, 2000, Loop Current rings and the deep circulation in the Gulf of Mexico, *Journal of Geophysical Research,* 105, 16951-16959.

Xu, Y., K.L. Tracey, D.R. Watts, M. Wimbush, W.J. Teague and J. Book, 2003, Current Meter Data Report: Ulleung Basin in the Japan/East Sea, *University of Rhode Island,* Graduate School of Oceanography Technical Report, 2003-02, 118pp.
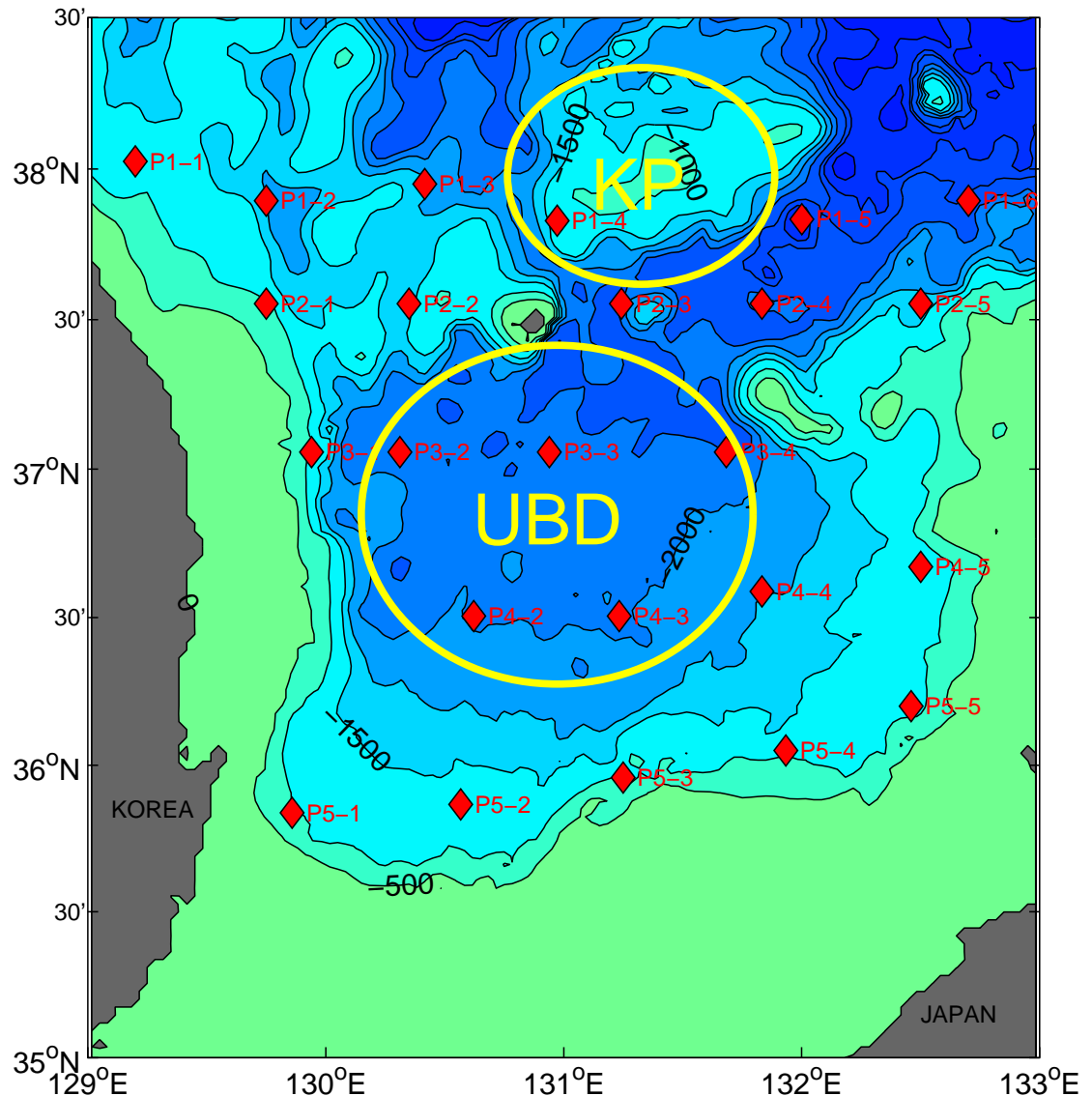
Figure 3.1. The southwestern Japan/East Sea. Diamonds indicate PIES sites. The PIES site identification numbers Pn-m are shown. Bathymetry contours are in meters. KP: Korea Plateau. UBD: Ulleung Basin Depression.
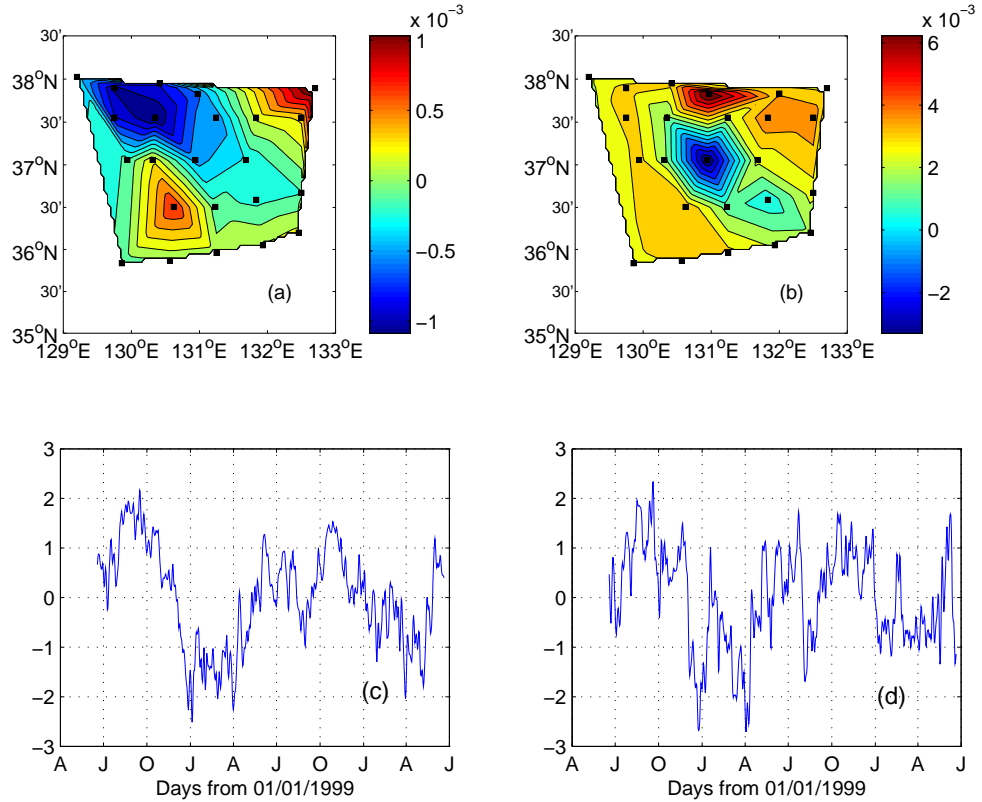
Figure 3.2. (a) and (b) respectively show the canonical maps of tau (unit: second) and bottom pressure (unit: dbar) for CCA1. (c) and (d) show respectively the temporal components. The canonical correlation is 0.75. CCA1 explains 10% of the tau variance and 31% of the bottom pressure variance.
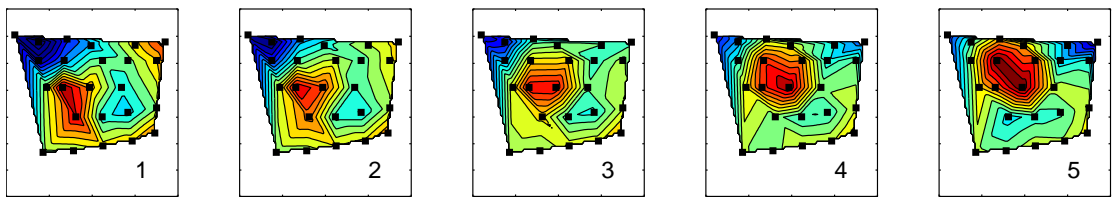
Figure 3.3. CCA1 maps of tau after restoring the time mean tau field. Maps 1-5 correspond respectively to different values of the time component: maximum, half of the maximum, zero, half of minimum and minimum. Hence the CCA1 represents variations in the tau field among these maps, which should be interpreted as a proxy for the upper baroclinic stream function and the mapped thermocline depth.
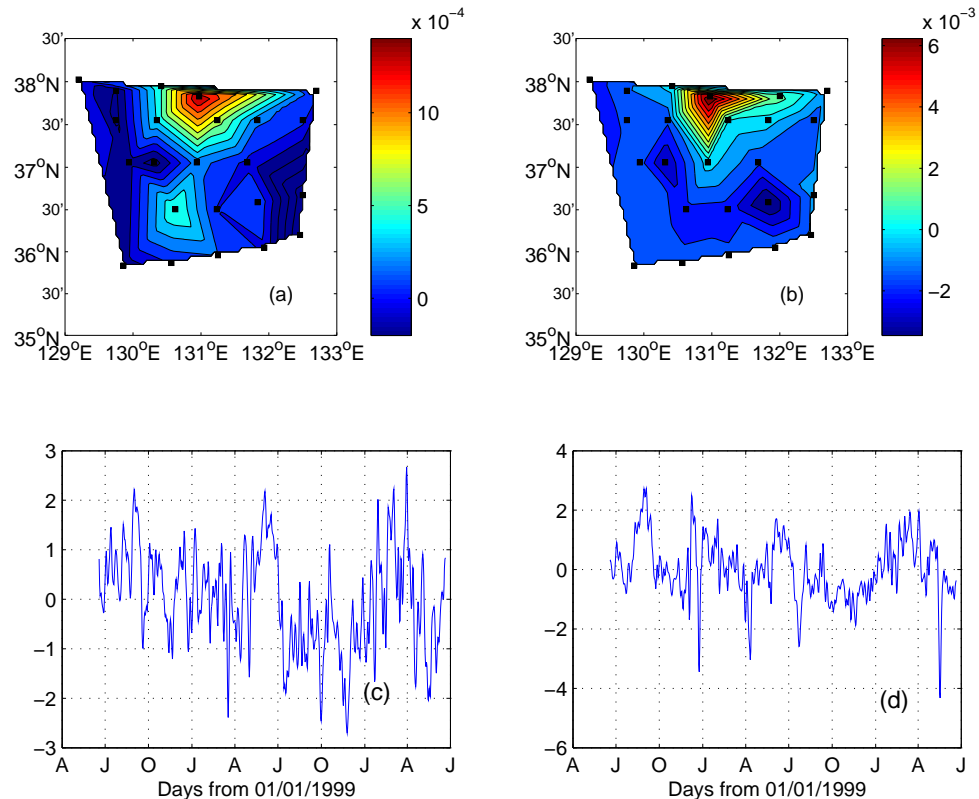
Figure 3.4. (a) and (b) show the canonical maps of tau (unit: second) and bottom pressure (unit: dbar) for CCA2. (c) and (d) show respectively the temporal components. The canonical correlation is 0.64. CCA2 explains 5% of the tau variance and 13% of the bottom pressure variance.
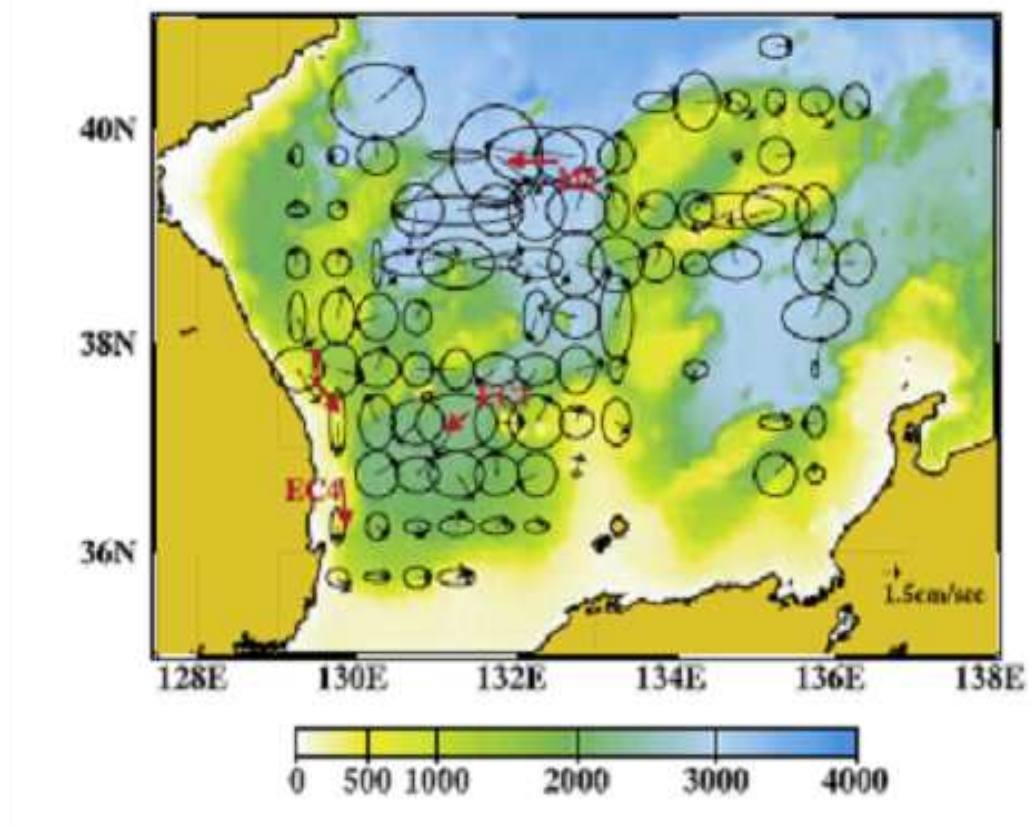
Figure 3.5. Mean velocity from intermediate level float data at 700 m by Park et al [2004]. The red arrows represent the mean flow vectors from the moorings.

APPENDIX A

On the sea level estimate from acoustic time measurements

It seems a paradox that the uncertainty of sea surface height (SSH) from PIES is 2.4 cm [Mitchell et al, 2004], while the scatter in acoustic travel time (τ) after reflection off the sea surface would suggest a larger uncertainty in SSH if it were estimated directly as a path length measurement from τ. In fact, the conversion process described below does not directly relate the estimate to the path length. Internal change in temperature and sound speed can cause much greater variation in τ in a water column that is greater than a few hundred meters depth. Consequently τ is instead used to estimate directly steric height which arises from density changes within the water column. Additional changes in sea level arising from changes of mass in the water column are determined from the bottom pressure (P_B) measurements.

Both τ and steric height can be derived from the temperature (T) and salinity (S) profiles. τ is determined by the equation:

$$\tau = 2 \times \int_0^{p_B} \frac{1}{\rho g c} dP \tag{A.1}$$

where g is gravity, P is pressure. The density ρ and sound speed c are functions of P, T and S. Steric height anomaly is defined as the sea level change associated with the integrated density change within the water column. The steric height anomaly ΔH expressed in meters is determined by the equation:

$$\Delta H = \frac{1}{g} \int_0^{p_B} \delta \, dP' \tag{A.2}$$

where δ represents the specific volume anomaly as a function of P, T, and S..

63

Using equations (A.1) and (A.2), τ and ΔH can be calculated with hydrographic casts that measure T(P) and S(P) profiles. Empirical relationships between τ and ΔH can be developed for a region, and for the JES Park et al [2005] further improved them by grouping hydrographic casts according to sea surface temperature (SST) and month. τ from PIES measurements can be combined with SST measurement from the daily maps of the TRMM satellite to look up an estimate of ΔH from these empirical relationships. Figure A.1 shows ΔH plotted against τ, calculated from equations (A.1) and (A.2) using about 520 hydrographic casts in the southwestern JES. The range of τ is about 10 ms, and the corresponding change in ΔH is about 30 cm.

In the following text we will estimate the uncertainty of τ measurements. The IES detector bandwidth is 150 Hz, determined by the electronics. The resolution (Δt) is limited by the frequency bandwidth (Δf), according to the uncertainty relation [Bendat and Piersol, 2002],

$$\Delta t > 1/(4\pi \times \Delta f) = 1/(4\pi \times 150) = 0.0005s = 0.5ms \qquad (A.3)$$

However time resolution of the echo detector (0.5 ms) is not the limiting factor that determines the scatter. The return echos are reflected off the sea surface, where surface waves cause scatter of individual echos much greater than the detector time resolution (A.3) because of multipath and constructive and destructive interference. The echo distribution typically has 2 ms standard deviation. The scatter mainly arises from the surface waves, and 2 ms is a representative standard deviation of individual τ measurements over a wide range of sea surface conditions (R.Watts, personal communication).

The IES measures 24 bursts of τ each hour with 10 second intervals within a single group. Typical surface gravity waves and swell have periods of 10 seconds

or less. The sampling interval for τ was chosen so that each pulse is scattered by independent uncorrelated ensembles of surface gravity waves. Thus the average τ would be improved by a factor of $\sqrt{24}$, and the uncertainty of the hourly averaged data would be about 2 ms $/\sqrt{24} \sim 0.4$ ms rms. Our processing algorithm selects the front edge of the distribution of echoes rather than a simple average, but this straightforward 0.4 ms uncertainty estimate for hourly τ illustrates sufficient accuracy for conversion to ΔH. τ was further 5 day low-pass filtered to monitor mesoscale steric height signals. The hourly τ values are observed to be approximately randomly distributed about a slowly varying signal. The 5-day low-pass (5DLP) has $5 \times 24 = 120$ hourly values, and its rms uncertainty should be further reduced by a factor of $\sqrt{120}$: 0.4 cm $/\sqrt{120} \sim 0.04$ ms which is our predicted standard deviation uncertainty for the 5DLP τ signal. Compared with the range of τ (10 ms) in Figure A.1, the uncertainty of τ (~ 0.04 ms) is small after 5-day low-pass filtering.

In the deep ocean, the temperature and density change within the water column accounts for most of the slowly varying change in τ. The steric height ΔH may be estimated from τ using the fitted curve in Figure A.1. The uncertainty in estimated ΔH arises both from the propagation of error due to the uncertainty in τ and from the intrinsic scatter of ΔH points about the fitted lookup curve. The uncertainty of τ mainly arises from the surface waves. In Figure A.1, the slope $\Delta H / \tau$ is approximately 3 cm/ms, so the propagation of τ error corresponds to only $3 \times 0.04 = 0.12$ cm contribution to the uncertainty of ΔH in the southwestern Japan/East Sea. The main uncertainty in ΔH is not from the uncertainty of τ, but from the uncertainty due to scatter of the empirical relations, which is about 2.2 cm in Figure A.1.
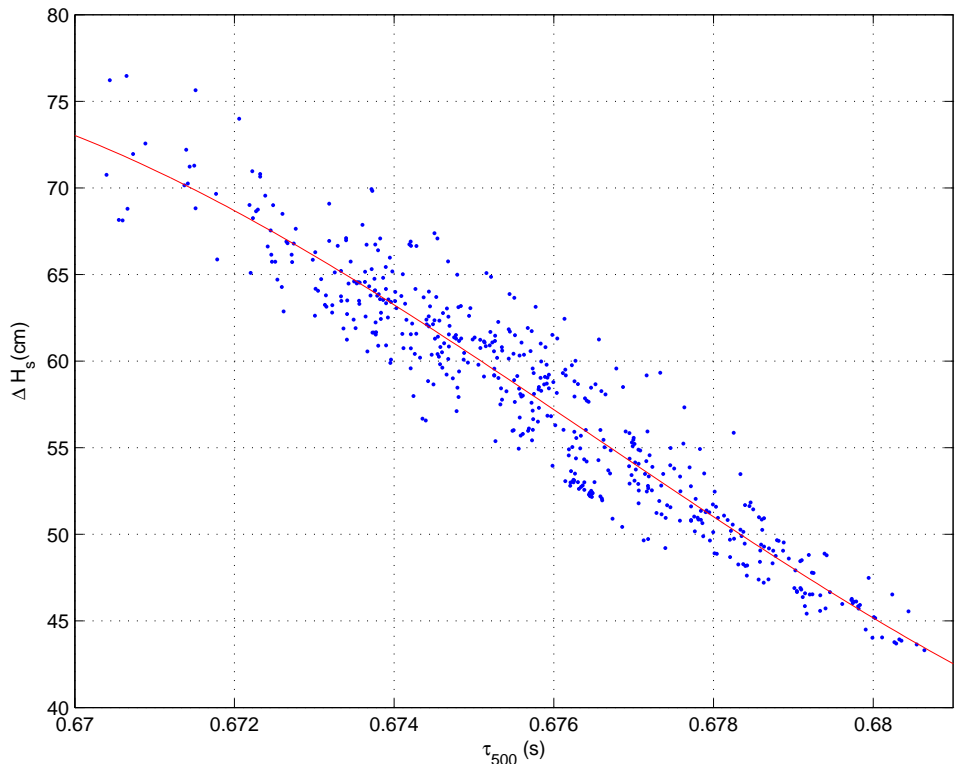
Figure A.1. Steric height anomaly at the surface relative to 500 db vs the simulated round trip acoustic travel time between the surface and 500 db. Quantities were determined from about 520 historical CTD casts in the southwestern Japan/East Sea. The CTD casts were grouped as described in the text according to SST ($< 22°C$) and month (June, July and August). The rms scatter of ΔH about the fitted curve is 2.2 cm.

APPENDIX B

Coherence between hourly Korea Strait transport and the amplitude of the basin oscillations

As an effort to investigate the energy sources of the basin-mode oscillations in the JES, we examined the coherence between the hourly Korea Strait transport and hourly bottom pressure at PIES site 6 near the mouth of the Korea Strait. The hourly Korea Strait transport was calculated by integrating the transport normal to a moored line of six acoustic Doppler Current Profiler (ADCP) moorings across the northern Korea Strait. The ADCP data, acquired from the Naval Research Laboratory, are those used in Teague et al [2002].

The coherence and phase between hourly Korea Strait transport and the bottom pressure at PIES site 6 near the mouth of the Korea Strait was computed for 50% overlapped segments each having 448 hourly data points, and the ensemble-average was calculated over all segments. The length of segment was selected as a near multiple of the M_2 tidal period, 12.42 hours, so that this strong tidal peak would be a harmonic in the Fourier analysis. The result is shown in Figure B.1. Coherence peaks are observed at tidal periods of K_1, M_2, M_3, M_4 and M_6, which are respectively 24.84hr, 12.42hr, 8.28hr, 6.21hr and 4.14hr. The phase is stable near each of these peaks, and in addition the phase is changing slowly between the M_3 and M_4 peaks, where the basin mode exists. But there is no coherence peak between M_3 and M_4 in that basin mode frequency band ($\sim$7hr) and the coherence in this band in insignificant. This shows that the basin mode is not driven significantly by fluctuations in Korea Strait transport (nor do the small variations of SSH from basin oscillations cause significant variations in KS transport.)

67
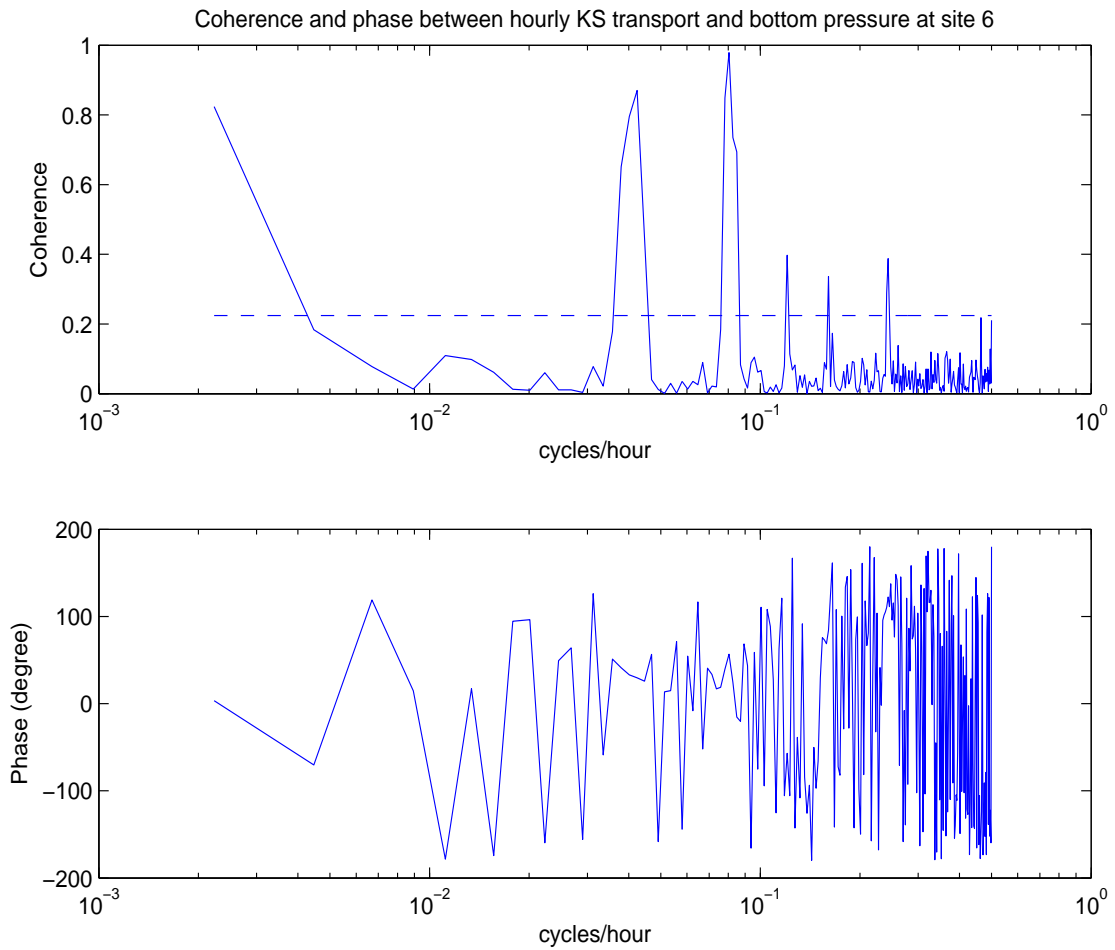
Figure B.1. Coherence and phase between hourly Korea Strait transport and bottom pressure at PIES site 6. Coherence peaks are labelled with their tidal constituent names. Dashed line in upper panel indicates the 95% confidence level of coherence.

APPENDIX C

Seismic events and the basin oscillations in the Japan/East Sea

We investigated earthquakes (Mag>5.5) in the Japan/East sea region during the two-year (1999-2001) period of the study in the Japan/East Sea. The data were acquired from Incorporated Research Institutions for Seismology (http://www.iris.edu/quakes/quakes.htm). Time, location, depth, and size of seismic events are listed in Table C.1. The seismic events and the amplitude of basin mode oscillations are shown in Figure C.1. Three earthquakes coincide with isolated minor peaks in CEOF amplitudes of the 7hr basin mode oscillations (2000/10/05, 2000/02/13 and 2000/11/23). But eleven earthquakes have no corresponding peaks in the basin mode amplitude.

Overall, seismic events during 1999-2001 can account for a very minor fraction of the variance of the basin mode oscillations
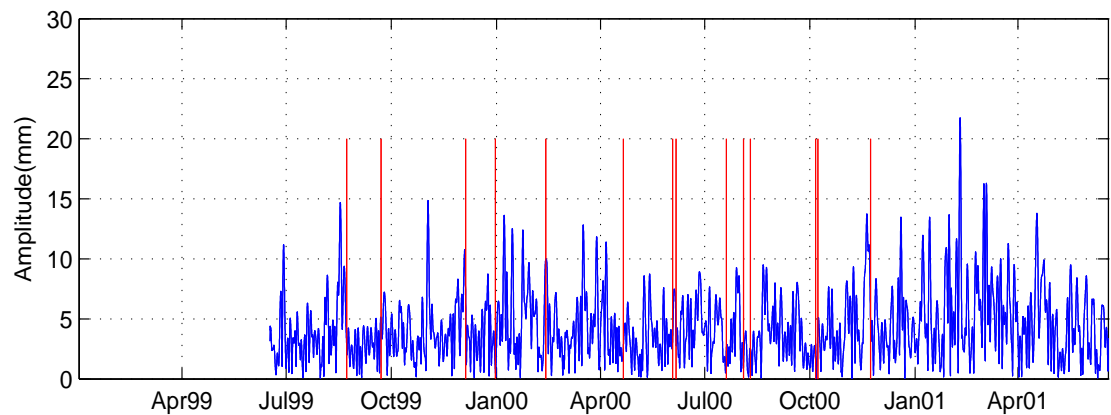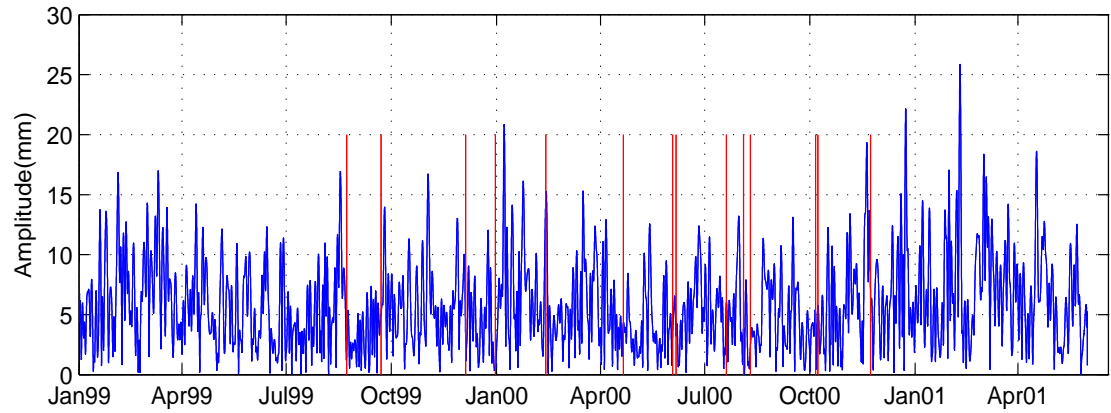
Figure C.1. Time series of CEOF (blue) and earthquakes (red). Upper panel: for the tide station data. Lower panel: for bottom pressure data

Table C.1. Time, location, depth, and size of seismic events in the Japan/East Sea during from June 1999 to June 2001

Time	LAT (N)	LON (E)	DEP (km)	SIZ (mag)
2000/11/23	44.58	138.83	264.9	5.8
2000/10/08	35.12	133.08	10.6	5.5
2000/10/06	35.38	133.16	0.6	5.7
2000/08/10	48.73	142.27	13.3	6.5
2000/08/04	48.75	142.24	13	7
2000/07/20	36.49	140.94	51	5.8
2000/06/06	36.82	135.51	2.3	5.7
2000/06/03	35.51	140.44	61.3	5.6
2000/04/21	35.66	135.52	351.4	5.8
2000/02/13	42.86	131.68	501.5	5.9
1999/12/31	37.28	134.63	376.8	5.8
1999/12/05	42.50	139.00	214.5	5.9
1999/09/22	45.57	142.63	295.5	5.6
1999/08/23	42.00	142.57	62	5.5

APPENDIX D

Canonical correlation analysis

Canonical correlation analysis can be defined as the problem of finding two sets of basis vectors, one for X and the other for Y, such that the correlations between the projections of the variables onto these basis vectors are mutually maximized. Canonical correlation can be derived in several ways. This appendix presents the eigenanalysis which had been described by Gittins [1985].

$X(q \times n)$ and $Y(p \times n)$ are observations on two sets of variables, where q and p are the number of variables for X and Y, and n is number of observations. The transpose and inverse of X are written as X^t and X^{-1}. We define covariance matrices:

$$S_{11} = XX^t, \quad S_{12} = XY^t, \quad S_{21} = YX^t, \quad S_{22} = YY^t \tag{D.1}$$

We seek linear transformations using $a(q \times 1)$ and $b(p \times 1)$,

$$u = a^t \cdot X, \quad v = b^t \cdot Y \tag{D.2}$$

such that the correlation between u and v is maximized. The correlation r between u and v expressed as a function of a and b is

$$r(a, b) = \frac{cov(a^t X, b^t Y)}{[var(a^t X)var(b^t Y)]^{1/2}} = \frac{a^t S_{12} b}{[(a^t S_{11} a)(b^t S_{22} b)]^{1/2}} \tag{D.3}$$

For convenience, it is customary to normalize a and b so that u and v have unit variance. Then

$$var(u) = a^t S_{11} a = 1, \quad var(v) = b^t S_{22} b = 1. \tag{D.4}$$

Expression (D.3) now reduces to

$$r(a, b) = a^t S_{12} b \qquad (D.5)$$

The algebraic problem therefore is to find a and b to maximize (D.5) subject to (D.4). Writing $\xi(a, b)$ for the function to be maximized under constraints (D.4)

$$\xi(a, b) = r(a, b) - 0 = a^t S_{12} b - \frac{1}{2}\lambda(a^t S_{11} a - 1) - \frac{1}{2}\mu(b^t S_{22} b - 1) \qquad (D.6)$$

where λ and μ are Lagrange multipliers. Taking the partial derivatives of ξ with respect to first a and then b and equating to the null vector we obtain

$$\frac{\partial \xi}{\partial a} = S_{12} b - \lambda S_{11} a = 0 \qquad (D.7)$$

$$\frac{\partial \xi}{\partial b} = S_{12}^t a - \mu S_{22} b = 0 \qquad (D.8)$$

Premultiplying (D.7) by a^t and (D.8) by b^t gives

$$a^t S_{12} b - \lambda a^t S_{11} a = 0 \qquad (D.9)$$

$$b^t S_{12}^t a - \mu b^t S_{22} b = 0 \qquad (D.10)$$

Using constraint (D.4), equations (D.9) and (D.10) give

$$a^t S_{12}^t b = \lambda = \lambda^t = (a^t S_{12}^t b)^t = b^t S_{12} a = \mu \qquad (D.11)$$

from (D.7), (D.8) and noting that $\lambda = \mu$ we have

$$S_{12} b = \lambda S_{11} a \qquad (D.12)$$

$$S_{12}^t a = \lambda S_{22} b \qquad (D.13)$$

73

Multiplying (D.12), (D.13) on the left by respectively $S_{21}S_{11}^{-1}$, $S_{12}S_{22}^{-1}$ gives

$$S_{21}S_{11}^{-1}S_{12}b = \lambda S_{12}^t a \qquad (D.14)$$

$$S_{12}S_{22}^{-1}S_{21}a = \lambda S_{12}b \qquad (D.15)$$

Substituting (D.12)·λ and (D.13)·λ respectively into (D.15) and (D.14) yield the equations

$$(S_{12}S_{22}^{-1}S_{21} - \lambda^2 S_{11})a = 0 \quad \text{or} \quad S_{11}^{-1}S_{12}S_{22}^{-1}S_{21}a = \lambda^2 a \qquad (D.16)$$

$$(S_{21}S_{11}^{-1}S_{12} - \lambda^2 S_{22})b = 0 \quad \text{or} \quad S_{22}^{-1}S_{21}S_{11}^{-1}S_{12}b = \lambda^2 b \qquad (D.17)$$

The eigenvectors of equations (D.16) and (D.17) are a_k and b_k, and they share the same eigenvalues λ_k, ($k \leq min(p,q)$ for non-zero solutions).

For n observations, u and v can be regarded as time series which have maximized correlation. The corresponding spatial patterns, A and B, are obtained by:

$$A = S_{11}a \qquad (D.18)$$

$$B = S_{22}b \qquad (D.19)$$

Thus X and Y can be reconstructed from the product of the spatial patterns (A and B) and the corresponding time series (u and v)

$$X = A \cdot u = (S_{11}a)(a^t X) = (a^t)^{-1}a^t X = X, \qquad (D.20)$$

$$Y = B \cdot v = (S_{22}b)(b^t Y) = (b^t)^{-1}b^t Y = Y \qquad (D.21)$$

where the normalization in equation (D.4) has been used. A and B are regarded as coupled patterns since their corresponding series u and v have maximized correlation.

APPENDIX E

First four EOF patterns of bottom pressure data

Figure E.1 shows the spatial patterns of the first four EOFs of bottom pressure. Their eigenvalues represent respectively 31%. 13%, 10%, and 8% of the variance. One criterion to indicate the robustness of EOF modes is that their eigenvalues should differ by at least a factor of two from the eigenvalues of the next greater and the next smaller mode. Clearly only EOF1 satisfies this criterion. However we choose to also examine EOF2 because its spatial structure is simple: one strongly positive region including five PIES sites, and a large nearly uniform negative region for all other sites. In contrast, the higher modes EOF3 and EOF4 exhibit spatially disorganized structures with random appearing spots centered on many neighboring PIES sites. So we chose to retain EOF2 and discard EOF3 and higher modes with disorganized structures in the bottom pressure fields. To minimize the influence from the higher modes, only the first two modes were retained in the prefiltering, as recommended for Canonical Correlation Analysis.
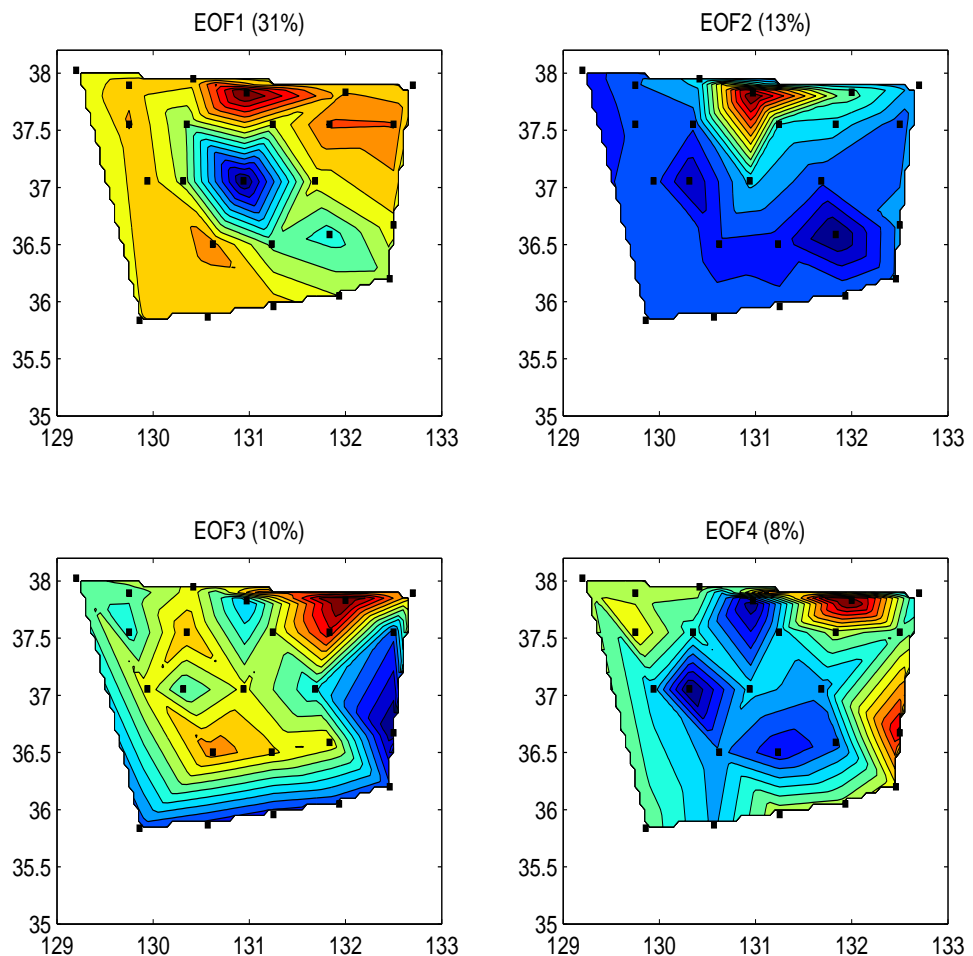
Figure E.1. First four EOF patterns of bottom pressure data. The variance of each mode is noted.

APPENDIX F

Robustness test of the CCA modes

To test the statistical robustness of the Canonical Correlation Analysis (CCA) patterns, we apply the CCA on the data subsampled with different time intervals. The estimated integral time scale of bottom pressure data is eighteen days.

The bottom pressure and tau data were five-day, ten-day and eighteen-day low pass filtered, and then subsampled correspondingly at two-day, five-day and nine day intervals. To avoid aliasing, the sampling time interval should be no larger than half of the low-pass cut-off period.

The CCA modes for the data with different sampling time intervals are shown in Figure F.1, F.2 and F.3. The CCA modes exhibit similar patterns for differently filtered data. The canonical correlations increase with the larger sampling time interval, while probability values of the chi-squared test statistic [Jobson, 1992] remain smaller than 0.05 indicating that these modes could occur from random data. These results suggest the robustness of the CCA modes.
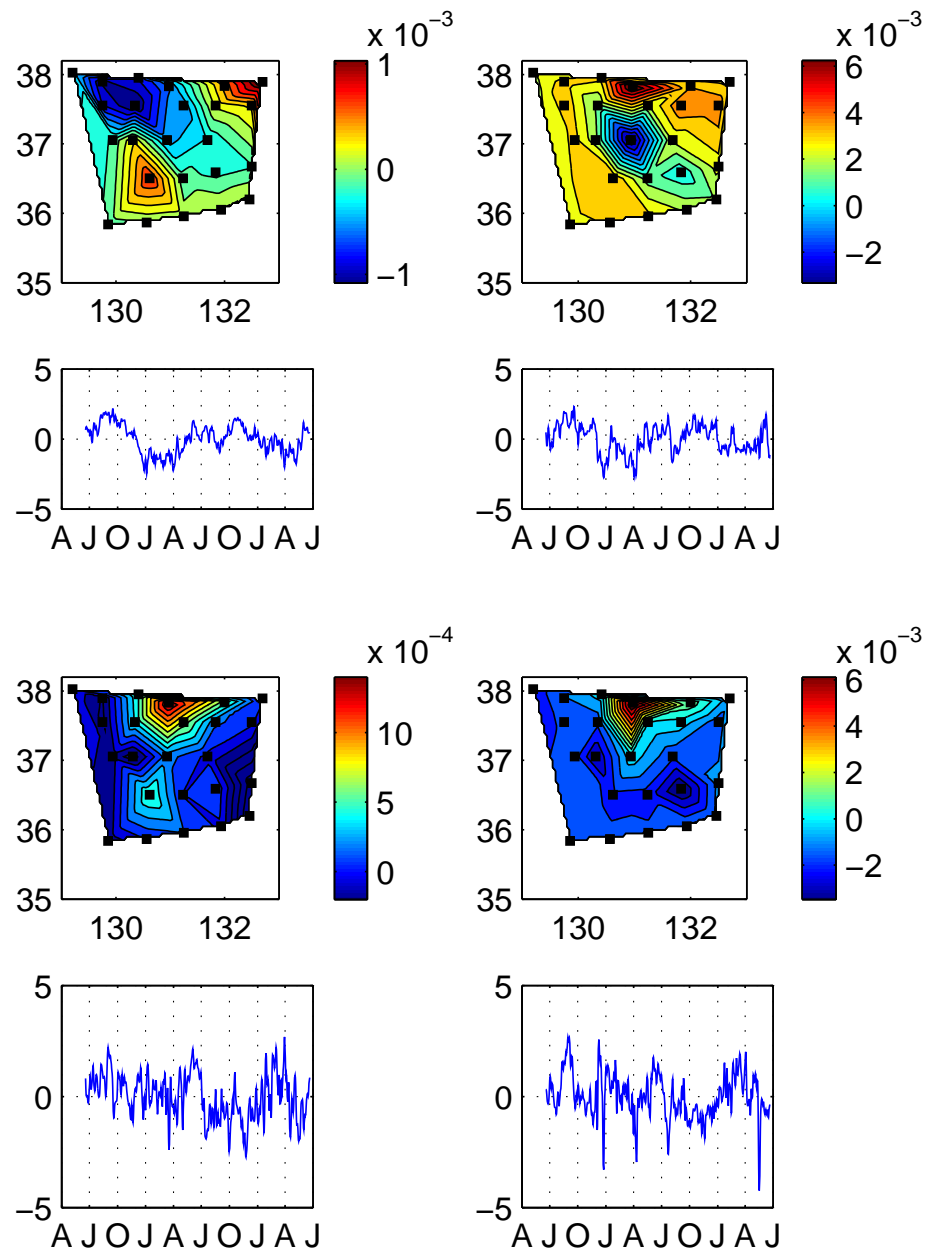
Figure F.1. The CCA modes for the data which is five-day low-pass filtered and subsampled with two day intervals. Upper panel: CCA1. Lower panel: CCA2. The canonical correlations of CCA1 and CCA2 are 0.75 and 0.64, respectively. The units for maps of tau (left panel) are seconds. The units for maps of pressure (right panel) are dbar.
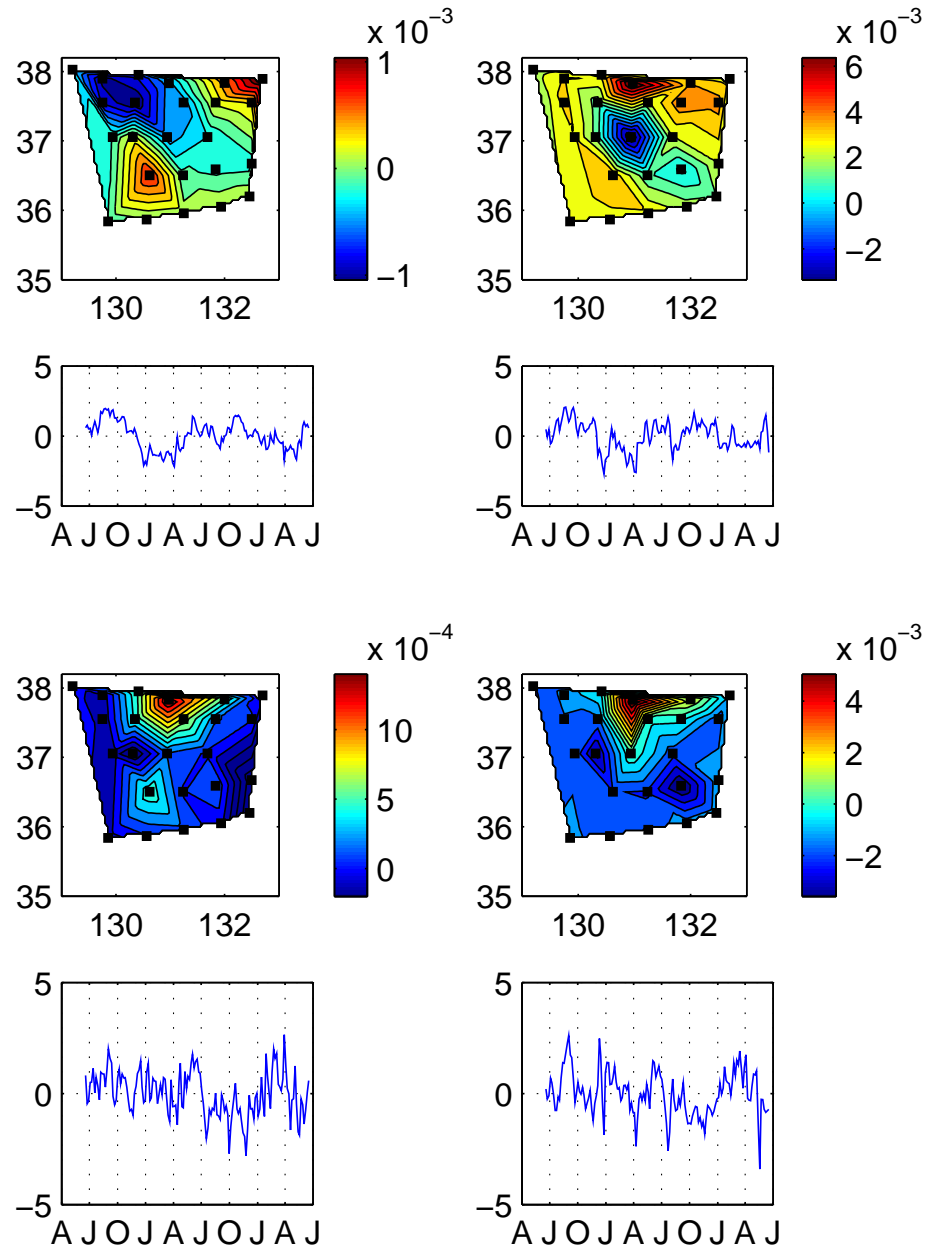
Figure F.2. The CCA modes for the data which is ten-day low-pass filtered and subsampled with five day intervals. Upper panel: CCA1. Lower panel: CCA2. The canonical correlations of CCA1 and CCA2 are 0.78 and 0.70, respectively. The units for maps of tau (left panel) are seconds. The units for maps of pressure (right panel) are dbar.
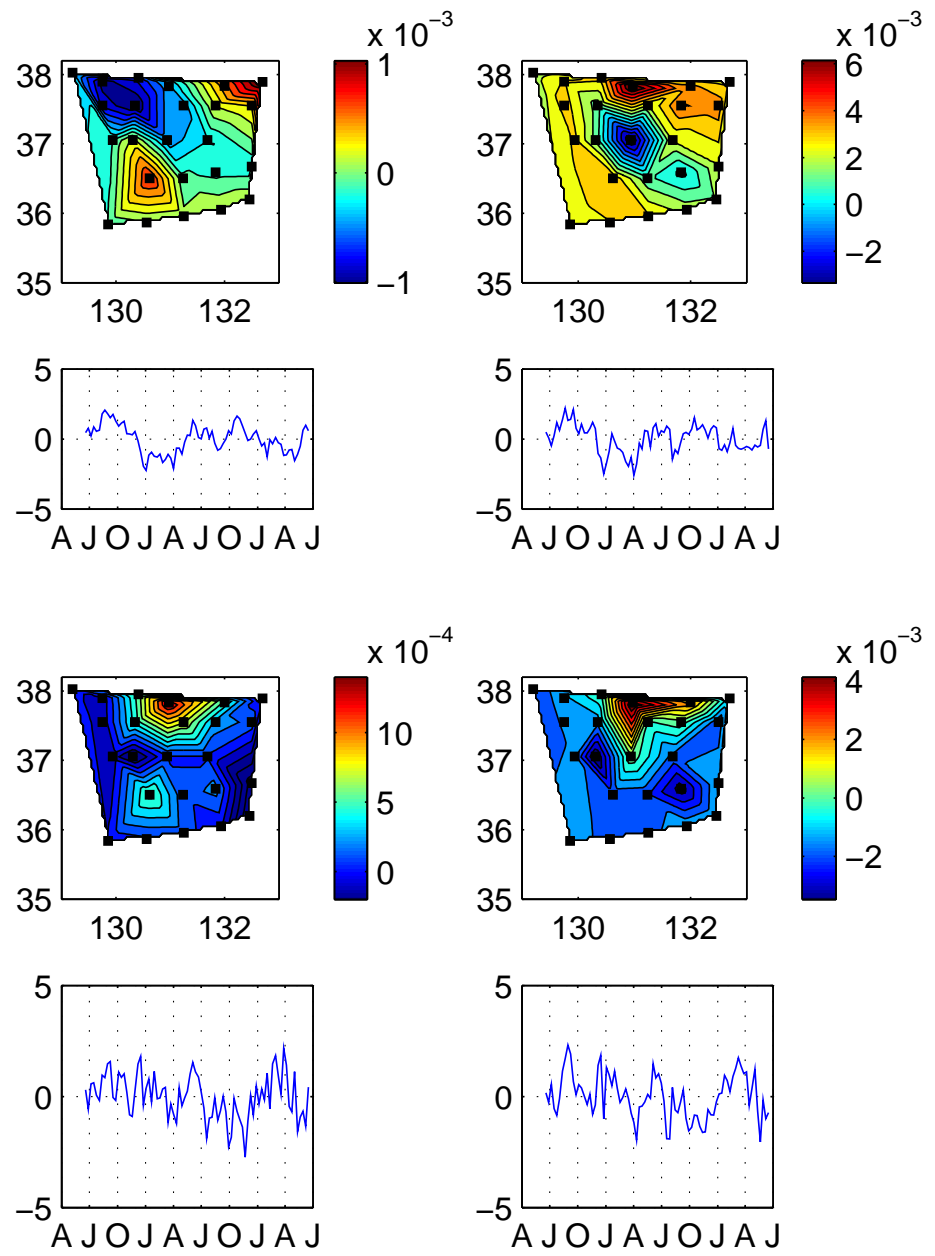
Figure F.3. The CCA modes for the data which is eighteen-day low-pass filtered and subsampled with nine day intervals. Upper panel: CCA1. Lower panel: CCA2. The canonical correlations of CCA1 and CCA2 are 0.82 and 0.79, respectively. The units for maps of tau (left panel) are seconds. The units for maps of pressure (right panel) are dbar.

BIBLIOGRAPHY

Barnett T.P., and R.W. Preisendorfer, 1987, Origins and levels of monthly and seasonal forecasts skill for United States surface air temperature determined by canonical correlation analysis, *Monthly Weather Review,* 115, 1825-1850.

Bendat, J.S., and A.G. Piersol, 2000, Random data analysis and measurement procecedures, 3rd Edition, *New York: Jonh Wiley and Son Inc.,* 155pp.

Bretherton, C.S., C. Smith, and J.M. Wallace, 1992, An intercomparision of methods for finding coupled patterns in climate data, *Journal of Climate,* 5, 541-560.

Byun, S.-K., C. Kim, K.-I. Chang and D. Jeon, 1997, Hydrographic characteristics observed near Ulreung Island in summer 1996, *Proceedings of the CREAMS'97 International Symposium,* Fukuoka, Japan, 89-91.

Chang, K.-I., W.J. Teague, S.J. Lyu, H.T. Perkins, D.-K. Lee, D.R. Watts, Y.B. Kim, D.A. Mitchell, C.-M. Lee, and K. Kim, 2004, Circulation and currents in the southwestern East/Japan Sea: Overview and review, *Progress in Oceanography,* 61, 105-156.

Cerovecki, I, M. Orlic and M.C. Hendershott, 1997, Adriatic seiche decay and energy loss to the Mediterranean, *Deep-Sea Research I,* 44, 2007-2029.

Cushman-Roisin, B., E.P. Chassignet, and B. Tang, 1990, Westward motion of mesoscale eddies, *Journal of Physical Oceanography,* 20, 758-768.

Ducet, N., and P.Y. Le Traon, 2000, Global high-resolution mapping of ocean circulation from TOPEX/Poseidon and ERS-1 and -2, *Journal of Geophysical Research,* 105, 19477-19498.

Emery, W.J., and R.E. Thomson, 2001, Data analysis methods in physical oceanography, 2nd Edition, *Elsevier Science Inc.,* 638 pp.

Frolov, S.A., G.G. Sutyrin, G.D. Rowe, and L.M. Rothstein, 2004, Loop Current Eddy Interaction with the Western Boundary in the Gulf of Mexico, *Journal of Physical Oceanography,* 34, 2223-2237.

Garrett, C., 1983, Variable sea level and strait flows in the Mediterranean: a theoretical study of the response to meteorological forcing, *Oceanologica Acta,* 6, 79-87.

Gittins, R., 1985, Canonical Analysis, *Berlin Heidelberg: Springer-Verlag,* 351pp.

Grinsted, A., J.C. Moore, and S. Jevrejeva, 2004, Application of the cross wavelet transform and wavelet coherence to geophysical time series, *Nonlinear Processes in Geophysics,* 11, 561-566.

Hallberg, R., 1997, Localized coupling between surface and bottom intensified flow over topography, *Journal Physical Oceanography,* 27, 977-999.

Hendry, R. M., D.R. Watts, and C.S. Meinen, 2002, Newfoundland Basin sea-level variability from TOPEX/POSEIDON altimetry and inverted echo sounder-bottom pressure measurements, *Canadian Journal of Remote Sensing,* 28, 544-555.

Hogan, P.J., and H.E. Hurlburt, 2000, Impact of upper ocean-topography coupling and isopycnal outcropping in Japan/East Sea models with 1/8° to 1/64° resolution, *Journal of Physical Oceanography,* 30, 2535-2561.

Hurlburt, H. E., 1986, Dynamic transfer of simulated altimeter data into subsurface information by a numerical ocean model, *Journal Geophysical Research,* 91, 2372-2400.

Indest, A.W., 1992, Ring dynamics in the western Gulf of Mexico, Ph.D. thesis, *Old Dominion Univversity,* Norfolk, Virginia, 127pp.

Jobson, J.D., 1992, Applied multivariate data analysis, *New York: Springer-Verlag,* 731pp.

Katz, E.J., 1997, Waves along the equator in the Atlantic, *Journal of Physical Oceanography,* 27, 2536-2544.

Lie, H.-J., S.-K. Byun, I. Bang and C.-H. Cho, 1995, Physical structure of eddies in the southwestern East Sea, *Journal of Korean Society Oceanography,* 30, 170-183.

Leder, N., and M. Orlic, 2004, Fundamental Adriatic seiche recorded by current meters, *Annales Geophysicae,* 22, 1449-1464.

Lyu, S.J., and K. Kim, 2005, Subinertial to interannual transport variations in the Korea Strait and their possible mechanism, *Journal of Geophysical Research,* 110, C12016, doi:10.1029/2004JC002651.

Metzner, M., M. Gade, I. Hennings, and A. B. Rabinovich, 2000, The observation of seiches in the Baltic Sea using a multi data set of water level, *Journal of Marine Systems,* 24, 67-84.

Mitchell, D.A., M. Wimbush, D.R. Watts, G. Sutyrin and W.J. Teague, 2004, The Residual GEM technique and its application to the southwestern Japan/East Sea, *Journal of Atmospheric and Oceanic Technology,* 21, 1895-1909.

Mitchell, D.A., J.W. Book, K.-I. Chang, M.-S. Suk, W.J. Teague, K.L. Tracey, D.R. Watts, M. Wimbush and J.-H. Yoon, 2005, Upper circulation patterns in the southwestern Japan/East Sea, *Deep-Sea Research II,* 52, 1617-1638.

Mitchell, D.A., Y. Xu, K.L. Tracey, D.R. Watts, M. Wimbush, and W.J. Teague, 2004, PIES Data Report: Ulleung Basin in the Japan/East Sea, *University of Rhode Island,* Graduate School of Oceanography Technical Report, 2004-02, 98pp.

Mitchell, D.A., W.J. Teague, M. Wimbush, D.R. Watts, and G.G. Sutyrin, 2005, The Dok Cold Eddy, *Journal of Physical Oceanography,* 35, 273-288.

Morimoto, A., T. Yanagi, and A. Kaneko, 2000, Tide correction of Altimetric data in the Japan Sea, *Journal of Oceanography,* 56, 31-41.

Morimoto, A., T. Yanagi, and A. Kaneko, 2000, Eddy field in the Japan Sea derived from satellite Altimetric data, *Journal of Oceanography,* 56, 449-462.

Munk, W.H., and D.E. Cartwright, 1966, Tidal spectroscopy and prediction, *Philosophical Transactions Royal Society London,* 259, 533-581.

Nam, S.-H., S.J. Lyu, Y.-H. Kim, K. Kim, J.-H. Park, and D.R. Watts, 2004, Correction of TOPEX/POSEIDON altimeter data for nonisostatic sea level response to atmospheric pressure in the Japan/East Sea, *Geophysical Research Letters,* 31, L02304, doi: 10.1029/2003GL018487.

Park, Y.-G., K.-H. Oh, K.-I. Chang, and M.-S. Suk, 2004, Intermediate level circulation of the southwestern part of the East/Japan Sea estimated from autonomous isobaric profiling floats, *Geophysical Research Letters,* 31, L13213, doi:10.1029/2004GL020424.

Park, J.-H., and D.R. Watts, 2005, Response of the southwestern Japan/East Sea to the atmospheric pressure, *Deep-Sea Research II,* 52, 1671-1683.

Park, J.-H., D.R. Watts, K.L. Tracey, and D.A. Mitchell, 2005, A multi-index GEM technique and its application to the southwestern Japan/East Sea, *Journal of Atmospheric and Oceanic Technology,* 22, 1282-1293.

Park, J.-H., D.R. Watts, M. Wimbush, J.W. Book, K.L. Tracey and Y. Xu, 2006, Rapid variability and its links to mesoscale circulation in the Japan/East Sea: basin osciallations, internal tides, and near-inertial oscillations, *Oceanography,* 19, 48-57.

Platzman, G.W., 1972, Two-dimensional free oscillations in natural basins. *Journal of Physical Oceanography,* 2, 117138.

Rikiishi, K., 1986, Tides and natural oscillations in the Japan Sea, *Kaiyo Monthly,* 18, 447-445 (in Japanese).

SSALTO/DUACS User Handbook, 2004, (M) SLA and (M)ADT Near-Real Time and Delayed Time Products, SALP-MU-P-EA-21065-CLS, Edition 1.2, 42pp.

Stammer, D., C. Wunsch, and R.M. Ponte, 2000, De-aliasing of global high frequency barotropic motions in altimeter observations, *Geophysical Research Letters,* 27, 1175-1178.

Sturges, W., J. Evans, S. Welsh, and W. Holland, 1993, Separation of warm-core rings in the Gulf of Mexico, *Journal of Physical Oceanography,* 23, 250-268.

Sutyrin, G., G. Rowe, L. Rothstein, and I. Ginis, 2003, Baroclinic eddy interactions with continental slopes and shelves, *Journal of Physical Oceanography,* 33, 283-291.

Teague, W.J., Z.R. Hallock, G.A. Jacobs, and J.L. Mitchell, 1995, Kuroshio sea surface height fluctuation observed simultaneously with inverted echo sounders and TOPEX/POSEIDON, *Journal of Geophysical Research,* 100, 24987-24994.

Teague, W.J., G.A. Jacobs, H.T. Perkins, J. Book, K.-I. Chang, and M.-S. Suk, 2002, Low frequency current observations in the Korea Strait, *Journal of Physical Oceanography,* 32, 1621-1641.

Teague, W.J., K.L. Tracey, D.R. Watts, J.W. Book, K.-I. Chang, P.J. Hogan, D.A. Mitchell, M.-S. Suk, M. Wimbush and J.-H. Yoon, 2005, Observed deep circulation in the Ulleung Basin, *Deep-Sea Research II,* 52, 1802-1826.

Teague, W.J., S.J. Lyu, H.T. Perkins, D.-K. Lee, D.R. Watts, Y.B. Kim, D.A. Mitchell, C.-M. Lee, and K. Kim, 2004, Circulation and currents in the southwestern East/Japan Sea: Overview and review, *Progress in Oceanography,* 61, 105-156.

Tierney, C., J. Wahr, F. Bryan, and V. Zlotnicki, 2000, Short-period oceanic circulation: Implications for satellite altimetry, *Geophysical Research Letters,* 27, 1255-1258.

Thompson, L., 1995, The effect of continental rises on the wind driven ocean circulation, *Journal of Physical Oceanography,* 25, 1296-1316.

Torrence, C. and G.P. Compo, 1998, A practical guide to wavelet analysis, *Bulletin of the American Meteorological Society,* 79, 61-78.

Watts, D.R., X. Qian, K.L. Tracey, 2001, Mapping abyssal current and pressure fields under the meandering Gulf Stream, *Journal of Atmospheric and Oceanic Technology,* 18, 1052-1067.

Welsh, S., and M. Inoue, 2000, Loop Current rings and the deep circulation in the Gulf of Mexico, *Journal of Geophysical Research,* 105, 16951-16959.

Xu, Y., K.L. Tracey, D.R. Watts, M. Wimbush, W.J. Teague and J. Book, 2003, Current Meter Data Report: Ulleung Basin in the Japan/East Sea, *University of Rhode Island,* Graduate School of Oceanography Technical Report, 2003-02, 118pp.